

**Encapsulation of poorly water soluble drug into  
organic nanotube and evaluation of its  
pharmaceutical property**

2017

Nan Liu

# CONTENTS

ABSTRACT	-1-
INTRODUCTION	-7-
EXPERIMENTAL	-11-
RESULTS AND DISCUSSION	-17-
PART I      Encapsulation of IBU into ONT-1 and ONT-2	-17-
PART II     Evaluation of the molecular state of IBU-loaded ONT	-27-
PART III    Dissolution characteristics of IBU from each ONT	-52-
CONCLUSIONS	-57-
ACKNOWLEDGEMENTS	-59-
REFERENCES	-61-
LIST OF PUBLICATION	-69-
THESIS COMMITTEE	-70-

# ABSTRACT

## **【Introduction】**

A new class of host material containing organic nanotubes (ONTs) are formed by the self-assembly of amphiphilic molecules, which are composed of two hydrophilic head groups and a hydrophobic aliphatic chain. Since the surface properties of ONT are controllable by changing the modified groups of the amphiphile, ONTs are expected to be novel drug delivery carriers to achieve controlled drug release. In this study, two ONTs; ONT-1 and ONT-2, were investigated for encapsulating a poorly water soluble drug, ibuprofen (IBU). The inner surfaces of ONT-1 and ONT-2 are functionalized with either carboxyl groups or amino groups, respectively. Molecular states of the incorporated IBU on the outer surface of ONTs, as well as in their inner hollow nanospace, were investigated with multiple solid-state NMR measurements using the fast magic-angle spinning (MAS) techniques. Moreover, the dissolution of IBU from the ONT was evaluated and discussed based on the molecular states of IBU.

## **【Methods】**

ONT-1 an anionic inner surface composed of carboxyl groups and an outer surface of 2-*N*-glucosamide groups, and ONT-2 that contains a cationic inner surface composed of amino groups and an outer surface of 1-*N*-glucosamide groups were used. IBU and each

ONT were mixed with various weight ratios. The mixtures were dispersed in organic solvents, and then evaporated to obtain the evaporation samples (EVPs). Field emission-transmission electron microscopy (FE-TEM) measurement, powder X-ray diffraction (PXRD) measurement, differential scanning calorimetry (DSC) measurement, solid state NMR measurement, and dissolution test were used for analysis of IBU/ONT-1 EVP and IBU/ONT-2 EVP. For solid-state NMR measurements, two one-dimensional (1D)  $^{13}\text{C}$  pulse sequences; cross polarization (CP) method and single pulse (SP) method, and two-dimensional (2D)  $^1\text{H}$ - $^{13}\text{C}$  heteronuclear correlation (HETCOR) with 40 kHz rotation were utilized.

## **【Results & Discussion】**

### **1. Encapsulation of IBU into ONT-1 and ONT-2**

FE-TEM images showed that the tubular inner and outer diameter were similar between ONT-1 (7.3 and 14.4 nm) and ONT-2 (6.8 and 16.2 nm). From the PXRD and DSC measurements, ONT-2 encapsulated a larger amount of IBU than ONT-1. IBU content in ONT-1 and ONT-2 EVPs was plotted as a function of heat of fusion of IBU crystal on DSC curves. Maximum encapsulated amounts of IBU with ONT-1 and ONT-2 were about 9.1 wt% and 29.2 wt%, respectively. This result suggests that ONT-2 can encapsulate about 20 wt% more IBU than ONT-1.

## **2. Evaluation of the molecular state of IBU-loaded ONT**

### **2-1. Quantitative evaluation of IBU in the inner nanospace and the outer surface of ONTs**

The nuclei with low mobility are emphasized more in the CP spectra, while those with low and high mobility are detected in the SP spectra. IBU in IBU/ONT-1 and IBU/ONT-2 EVPs showed two families of peaks emphasized in either the CP or SP spectrum. The results indicated that the IBU with either lower mobility or higher mobility existed on the outer surface or in the inner hollow nanospace of ONTs, respectively. The encapsulation ratio of IBU was estimated using the peak area of C3 (“inner” and “outer”) after the process of the wave-form separation. As a result, the IBU encapsulation ratio in the inner nanospace versus that on the outer surface was calculated to be about 1 : 1 for ONT-1 and 2 : 1 for ONT-2. Thus, the IBU was more efficiently encapsulated in the hollow nanospace than on the outer surface for IBU/ONT-2 EVP. Meanwhile, for IBU/ONT-1 EVP, IBU encapsulation was equimolar in the inner hollow nanospace and at the outer surface. The difference in the encapsulated amounts could be explained by the different strength of interaction between IBU and the inner surfaces of the ONTs with different functional groups.

### **2-2. Interaction between IBU and ONT**

The changes in  $^{13}\text{C}$  chemical shifts and peak shapes of IBU carboxyl group in the inner nanospace of both ONT-1 and ONT-2 were larger than the other groups, indicating that IBU interacted with ONT inner surface mainly through the carboxyl groups of IBU. For IBU/ONT-1 EVP, IBU loading showed no changes in  $^{13}\text{C}$  peak of the inner surface of ONT-1. In contrast, significant changes of  $^{13}\text{C}$  peaks of ONT-2 were observed. The larger peak changes indicated stronger interactions between IBU and inner surface of ONT-2 compared to ONT-1.

The changes of  $^{13}\text{C}$  peak of the IBU carboxyl group and ONT glucose group on the outer surface of ONT were detected for both IBU/ONT-1 and IBU/ONT-2 EVPs. Furthermore, in the 2D  $^1\text{H}$ - $^{13}\text{C}$  HETCOR spectrum, both the EVPs clearly showed well-separated cross peaks between the carboxyl carbon of IBU and the hydroxyl proton of the glucose group in ONTs. The interaction at the outer surface between carboxyl carbon of IBU and the hydroxyl proton of the ONT glucose group was clearly demonstrated.

There are two types of spaces where IBU could be loaded: the hollow nanospace of an ONT and the outer surface of ONTs. In both the IBU/ONT-1 and IBU/ONT-2 EVPs, the IBU in the inner nanospace had much higher mobility, while IBU existed at the outer surface of the ONT was less mobile. The IBU in the inner hollow nanospace of

ONT-1 was weakly encapsulated via interactions between the carboxyl group of IBU and the inner surface. In contrast, those in IBU/ONT-2 EVP were strongly encapsulated in the inner hollow nanospace through electrostatic interactions of the IBU carboxyl group with the amino group on the inner surface of ONT-2. This stronger interaction could result in encapsulation of a larger amount of IBU in ONT-2 than ONT-1. At the outer surface, weak interaction was formed between the IBU carboxyl group and the ONT glucose group for both IBU/ONT-1 and IBU/ONT-2 EVPs.

### **3. Dissolution characteristics of IBU from each ONT**

IBU dissolved rapidly from ONT-1 compared to that from IBU crystals. On the other hand, IBU released from ONT-2 was significantly suppressed. IBU dissolution from each ONT was hypothesized based on the molecular interactions of IBU and different functional groups on the ONTs. Dissolution of IBU/ONT EVP shows three stages: (1) water penetration into both the inner hollow nanospace and the interstitial spaces between the ONTs, (2) dissolution of the IBU from the outer surface of ONT, and (3) dissolution of IBU from the inner hollow nanospace of the ONT. In the IBU/ONT-1 EVP, the interaction between IBU and ONT-1 in the inner nanospace was so weak that (2) and (3) occurred at the same time. Hence, almost all the IBU was rapidly released. On the other hand, in IBU/ONT-2 EVP, since IBU and ONT-2 displayed a strong

electrostatic interaction, the IBU in the inner nanospace was gradually released after the IBU on the outer surface was released.

### **【Conclusions】**

The molecular state of IBU/ONT EVP was quantitatively and qualitatively evaluated. This study clearly indicates the utility of functionalized ONTs as drug carriers that may allow controlled encapsulation and dissolution of poorly water-soluble drugs by changing the nature of the host-guest interactions.



## INTRODCTION

Organic nanotube (ONT), a new host material, is formed by the self-assembly of amphiphilic molecules which are composed of two hydrophilic head groups at the ends of a hydrophobic aliphatic chain. ONTs have an inner hollow nanospace whose size is meso-scale, depending on the amphiphilic species. Recent development of preparation technique of ONT has enables it to be produced easily and massively.<sup>1-3</sup> ONT possesses many advantages compared to other host materials, such as product safety, good dispersibility in water, and controllable size. These features have allowed an ONT to receive much attention as a promising host material for drug delivery system (DDS).

The nanoarchitecture with functionalized surface have been widely used in order to control drug encapsulation and dissolution. The inner surface of mesoporous matrices are functionalized with chemical groups that are able to interact with the drug molecules through ionic or hydrogen bond.<sup>4-7</sup> The effective drug encapsulation and controlled dissolution depending on the external environment changes (e.g. pH, temperature, and magnetic field) have been reported using the mesoporous materials with the functionalized surface.<sup>8,9</sup> The surfaces of ONT can be also designed with functional groups based on the chemical structures of the amphiphiles used.<sup>2</sup> Those ONTs with functional surface can selectively and effectively encapsulate water soluble materials

such as proteins,<sup>10,11</sup> DNA,<sup>12</sup> and doxorubicin (DOX)<sup>13</sup> into their hollow nanospace when they are dispersed in aqueous solution. This encapsulation is caused by the electrostatic interaction between each guest and the ONT inner surface. Furthermore, the drug dissolution from ONT is also controlled via external stimuli such as pH and temperature change.<sup>14</sup> In order to develop ONT as a drug carrier for poorly water-soluble drug, which occupies over 40% of recent drug candidates,<sup>15,16</sup> it is necessary to evaluate their physicochemical properties encapsulated in ONT. As above-mentioned, encapsulation and dissolution of a guest drug in ONT is influenced by the appropriate modification of the inner surface of the ONT. Here, it is expected that the changes of functional group of ONT surface can also control the encapsulation and dissolution of poorly water-soluble drugs.

In order to design the appropriate formulations using ONT, it is necessary to characterize the molecular state of a guest drug encapsulated in ONT and the various interaction between the drug and the host ONT. Moreover, it has also been observed that ONTs are able to encapsulate guest materials into not only the hollow nanospace of ONTs but also the interstitial space formed between ONTs.<sup>17,18</sup> Large guest materials such as metal nanoparticles and fluorescent proteins encapsulated inside the hollow nanospace have been studied by transmission electron microscopy (TEM) observation

and fluorescence microscopy,<sup>19-21</sup> though unequivocal evidence for the guest molecules loading in the interstitial space has not yet been reported. Moreover, it is difficult to evaluate the location of the encapsulated drugs whose sizes are smaller than large materials described above with TEM observation and fluorescence microscopy. Solid-state NMR technique have been widely used as a powerful tool to study the structure, molecular dynamics, and interactions of various host-guest system such as drug-cyclodextrin inclusion complex and drug-mesoporous material systems.<sup>22-24</sup> However, to our best knowledge, there are no detailed reports which describe the molecular state of guest drug and the interaction between guest drug and the surface of host ONT by solid-state NMR techniques, and, the location of the encapsulated drug within and on the ONT can be understood and studied through investigating the interaction between the drug and the ONT.

Herein, we described two ONTs with a similar tubular size and different functional groups on the inner and outer surfaces, into which a poorly water-soluble drug, ibuprofen (IBU) was encapsulated by an evaporative method using organic solvents.

In part I, the encapsulation of IBU into ONTs was evaluated. The morphology of ONT-1 and ONT-2 was observed by field emission-transmission electron microscopy (FE-TEM) and the encapsulation amount of IBU into each ONTs was determined by

powder X-ray diffraction (PXRD) and differential scanning calorimetry (DSC) measurements.

In part II, solid-state NMR study were carried out to characterize the molecular states of both the guest IBU and the host ONTs. High-resolution 1D  $^1\text{H}$  spectrum and two 1D  $^{13}\text{C}$  spectra by single pulse (SP) and cross polarization (CP) methods with fast magic-angle spinning (MAS) at 40 kHz were used to investigate the structure and molecular dynamics in detail. Additionally, 2D  $^1\text{H}$ - $^{13}\text{C}$  heteronuclear correlation (HETCOR) measurement were performed to assign all the  $^1\text{H}$  and  $^{13}\text{C}$  peaks of IBU and ONTs, and to investigate the intermolecular interactions between IBU and the inner and outer surface of each ONT.

In part III, dissolution characteristics of IBU from each ONT were studied and compared in order to assess the properties and feasibility of ONTs as functionalized drug carriers.

# EXPERIMENTAL

## Materials

*N*-{12-[(2- $\alpha$ , $\beta$ -D-glucopyranosyl)carbamoyl]dodecanyl}-glycylglycylglycine acid (glycolipid 1) and *N*-( $\beta$ -D-glucopyranosyl)-*N'*-(2-glycylglycylglycineamideethyl)-octadecanediamide (glycolipid 2) were prepared as reported previously.<sup>25,26</sup> ONT-1 and ONT-2 were formed by self-assembly of glycolipid 1 and glycolipid 2, respectively. Ibuprofen (IBU) was purchased from Wako Pure Chemical Industries, Ltd. (Kyoto, Japan). The chemical structures of the materials used in this study are represented in Figure 1.

## Preparation of ONT-1 and ONT-2

Glycolipid 1 and 2 were dispersed in distilled water at the concentration of 1.0 mg/mL by sonication and refluxed at 100 °C for 10 min. The hot resultant solutions of glycolipid 1 and 2 were gradually cooled down to room temperature. ONT-1 was obtained by freeze drying of glycolipid 1 solution via the freeze dryer FD-1000 (Rikakikai. Co., Ltd, Tokyo, Japan). For ONT-2, after cooling down to room temperature, the HCl salt glycolipid 2 was neutralized by NaOH solution (conc.: 2%

v/v) to a pH of about 7. Then, the solution was dialyzed against distilled water for 24 h and freeze dried to prepare ONT-2.

### **IBU loading into ONTs**

The mixture of IBU and ONTs with various weight ratio were dispersed in organic solvents at ONT concentration of 1 mg/mL in organic solvents. The organic solvent used for ONT-1 and ONT-2 was acetone and methanol, respectively. The mixtures were sonicated for 3 min. The solvents were removed by a rotary evaporator and then dried in vacuum to obtain evaporated samples (EVPs).

### **Field emission-transmission electron microscopy (FE-TEM)**

The ONTs were dispersed in water and dripped onto a standard TEM grid supported by Excel Support Film<sup>®</sup> (Cu 200, Nisshin EM Co. Ltd., Tokyo, Japan). ONTs were left to adsorb onto the grid for 3 min, and then the excess solution was blotted with filter paper. Each sample was negatively stained with 2 wt% phosphotungstate solution (pH 7.4) for 3 min. The grid was dried in a desiccator at room temperature for 1 day. FE-TEM observations were carried out at 120 kV using JEOL-JEM2100F (JEOL Ltd., Tokyo, Japan).

## **Powder X-ray diffraction (PXRD)**

PXRD measurements were performed using a Rigaku MiniFlex II powder diffraction system (Tokyo, Japan). The X-ray source was CuK $\alpha$  radiation (30 kV and 15 mA). The scanning range ( $2\theta$ ) was 2–35°, and the scan speed was 4°/min.

## **Differential scanning calorimetry (DSC)**

DSC measurements were carried out using a SII Nano Technology EXSTAR6000 DSC6200 (Tokyo, Japan). Samples (*ca.* 5 mg) were put into crimped aluminum pans. N<sub>2</sub> was used as the purge gas at a flow rate of 60 mL/min. The temperature range was 50–150 °C at a heating rate of 5 °C /min.

## **Solid-state NMR spectroscopy**

All solid-state NMR spectra were recorded by a Varian 600 MHz NMR spectrometer using a Varian 1.6 mm T3 NB triple resonance probe (Agilent Technology, California, USA) spinning at a MAS rate of 40 kHz, operating at 599.7 MHz for <sup>1</sup>H and 150.8 MHz for <sup>13</sup>C. The <sup>1</sup>H spectra were recorded under the following conditions: spectral width of 100 kHz, acquisition time of 100 ms, recycle delay time of 10 s, <sup>1</sup>H  $\pi/2$  pulse lengths of

1.3  $\mu$ s. The  $^{13}\text{C}$  CP/MAS spectra were measured under the following conditions: spectral width of 40 kHz, acquisition time of 40 ms, recycle delay time of 7 s, contact time of 3.5 ms,  $^{13}\text{C}$   $\pi/2$  pulse lengths of 1.6  $\mu$ s. The  $^{13}\text{C}$  SP/MAS spectra were obtained under the following conditions: spectral width of 40 kHz, acquisition time of 40 ms, recycle delay time of 5 s,  $^{13}\text{C}$   $\pi/2$  pulse lengths of 1.2  $\mu$ s. 2D  $^1\text{H}$ - $^{13}\text{C}$  HETCOR spectra were collected under the following conditions: acquisition time of 40 ms, recycle delay time of 7 s, contact time of 0.3–5 ms,  $^{13}\text{C}$   $\pi/2$  pulse lengths of 1.6  $\mu$ s,  $^1\text{H}$   $\pi/2$  pulse lengths of 1.3  $\mu$ s. Adamantane was used as a chemical shift reference at 38.52 ppm for  $^{13}\text{C}$  and 1.91 ppm for  $^1\text{H}$ . All experiments were performed with the inlet air temperature controlled at 10 °C.

## **Dissolution test**

The dissolution of IBU from EVPs were evaluated using the Japanese Pharmacopeia (JP) XVI paddle method with a dissolution tester NTR-VS6P (Toyama Sangyo Co. Ltd., Osaka, Japan). The IBU/ONT-1 = 1 : 9 (w/w) and IBU/ONT-2 = 3 : 7 (w/w) EVPs equivalent to 3 mg IBU were added to 300 mL acetic acid-sodium acetate buffer solution at pH 4.0. The paddles were rotated at 50 rpm at  $37.0 \pm 0.5$  °C. A sample volume of 3 mL was withdrawn from the dissolution medium at 3, 5, 10, 20, 30, 60 and



120 min. The samples were filtered by 0.20  $\mu\text{m}$  cellulose nitrate membrane filter and analyzed with HPLC. All dissolution tests were performed in three replicates.

### **HPLC analysis**

IBU was analyzed by a Hitachi HPLC system consisting of an L-6000 pump and an L-4000 UV-detector (Tokyo, Japan). The analysis was carried out on a TSK GEL ODS column (4.6 $\times$ 150 mm). The mobile phase consisted of a 50 : 50 (v/v%) mixture of acetonitrile and phosphoric acid solution at pH 3.0. The flow rate was 1.3 mL/min and the detection wavelength was 264 nm. The injection volume was 20  $\mu\text{L}$ .

### **Field emission-scanning electron microscopy (FE-SEM)**

The powder of each IBU/ONT EVP was mounted on an SEM stub using carbon adhesive tape and dried under vacuum for 24 h. The adhesive samples were coated with an osmium plasma coater Meiwafoxis Neoc-ST (MEIWAFOXIS. Co. LTD., Tokyo, Japan), and the thickness of the osmium coating was kept below 2.5 nm. FE-SEM was performed with a JEOL JSM-6330F (JEOL Ltd., Tokyo, Japan) using an acceleration voltage of 3.0 kV.

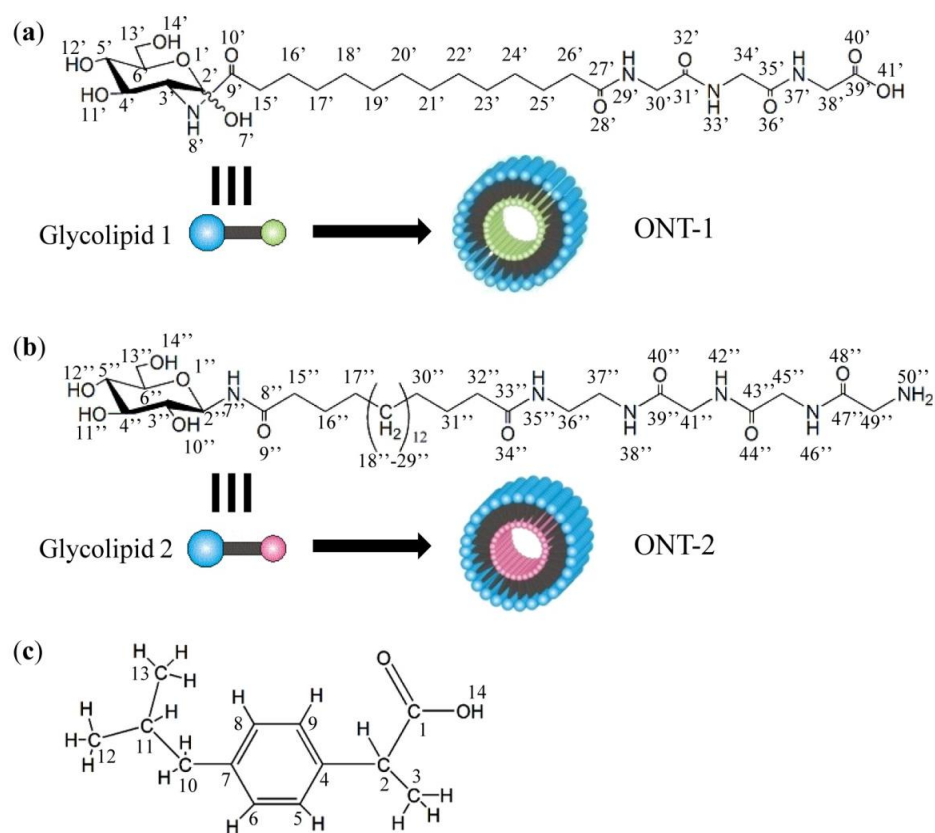


**Figure 1.** Chemical structures of (a) glycolipid 1, (b) glycolipid 2 and (c) ibuprofen (IBU). Glycolipid 1 and glycolipid 2 form ONT-1 and ONT-2 by the self-assembly, respectively.

# RESULTS AND DISCUSSION

## PART I Encapsulation of IBU into ONT-1 and ONT-2

### 1. Morphology of ONT-1 and ONT-2

The morphology and size of ONTs were evaluated by FE-TEM measurement (Figure 1-1). Both of ONT-1 and ONT-2 showed the tubular structure with the diameter in the nanometer gauge and the length in the  $\mu\text{m}$  gauge. The average outer and inner diameters of 250 species of ONTs were determined from FE-TEM images. ONT-1 consisted of tubular nanostructure with  $14.4 \pm 1.7$  nm outer diameter and  $7.3 \pm 0.7$  nm inner diameter. The outer diameter and inner diameter of ONT-2 was  $16.2 \pm 2.4$  nm and  $6.8 \pm 1.0$  nm, respectively. FE-TEM images showed that ONT-1 yielded tubular structure and hollow nanospace similar to ONT-2. It was confirmed that the tubular structure of both ONT-1 and ONT-2 was maintained after evaporation from organic solvent, acetone and methanol, respectively (Figure 1-2).

### 2. Preparation of IBU/ONT EVP

Ibuprofen (IBU) encapsulation into ONTs by evaporation method was evaluated by PXRD measurement. Figure 1-3 shows the PXRD patterns of the IBU/ONT EVPs with the various contents of IBU. The characteristic IBU peaks disappeared in the

IBU/ONT-1 EVPs with the IBU contents of 5 wt%~15 wt%, indicating that crystalline IBU changed to the amorphous one by evaporation with ONT-1 at IBU content less than 15 wt%. Moreover, evaporation with ONT-1 also changed the state of hydrocortisone (HCT) and phenytoin (PHE) from crystalline to amorphous by incorporation into ONT-1 with the drug contents of 30 wt% (Figure 1-4d, i).<sup>27</sup> Therefore, the amorphization of IBU was induced by incorporation into ONT structure. In contrast, diffraction peaks corresponding to excess IBU that had not been incorporated into ONT-2 were observed in IBU/ONT-2 EVPs with drug contents of 50 wt%~35 wt% (Figure 1-3 i-l). A halo pattern was observed in the diffraction pattern of IBU/ONT-2 EVP with drug contents of 30 wt% (Figure 1-3m). In ONT-2 EVPs with drug contents below 30 wt%, IBU was encapsulated into the ONT-2 structure. These PXRD experiments demonstrated that ONT-2 encapsulated IBU more efficiently than ONT-1.

### 3. Encapsulation amount of loaded IBU in ONT

The DSC measurement was carried out in order to determine the encapsulated amount of IBU in ONTs. (Figure 1-5) The DSC curves of IBU crystal exhibited an endothermic peak at 72 °C (onset temperature), which corresponds to its melting. In the DSC curves of IBU/ONT EVPs, no thermal events were detected in the DSC curves of ONT-1 and ONT-2 between 50 and 150 °C. No melting peak of IBU was observed in

the DSC curve from IBU/ONT-1 and IBU/ONT-2 EVP with the drug content of 5 wt% and 30 wt%, respectively. Drugs encapsulated as amorphous state into the mesopores show no melting peaks in the DSC curves.<sup>28</sup> The absence of IBU melting peak in the DSC curve of the EVPs indicated that IBU was in amorphous state due to encapsulation by ONTs. The amount of encapsulated IBU into ONTs was quantitatively determined by the heat of fusion of IBU melting peak on the DSC curves. Figure 1-6 shows the plotting of the heat of fusion against IBU content of EVPs. The heat of fusion of IBU melting in IBU/ONT-1 and IBU/ONT-2 EVPs were plotted as a function of IBU contents. The fitted lines to the plots in both the IBU/ONT-1 and IBU/ONT-2 EVPs showed good linearity with high correlation coefficient ( $R^2 > 0.99$ ). The Y-axis intercept values of each plot represent the maximum encapsulation amount of drug.<sup>29</sup> The maximum amount of IBU encapsulated into ONT-2 was at 29.2 wt% significantly higher than that 9.1 wt% in ONT-1. The inner diameters of tubular structure observed by FE-TEM images (Figure 1-1) were similar between ONT-1 and ONT-2. Thus, this difference of the encapsulated amount of IBU between ONTs could be attributed to the characteristic difference of substituent groups of ONT's inner surface.

In conclusions, IBU was successfully encapsulated into both of the ONTs via a solvent evaporation method. The loaded IBU existed as amorphous state in each ONT.

ONT-2 which contains amino groups on the inner surface can encapsulate about 20 wt% more IBU than ONT-1, which has carboxyl groups on the inner surface.

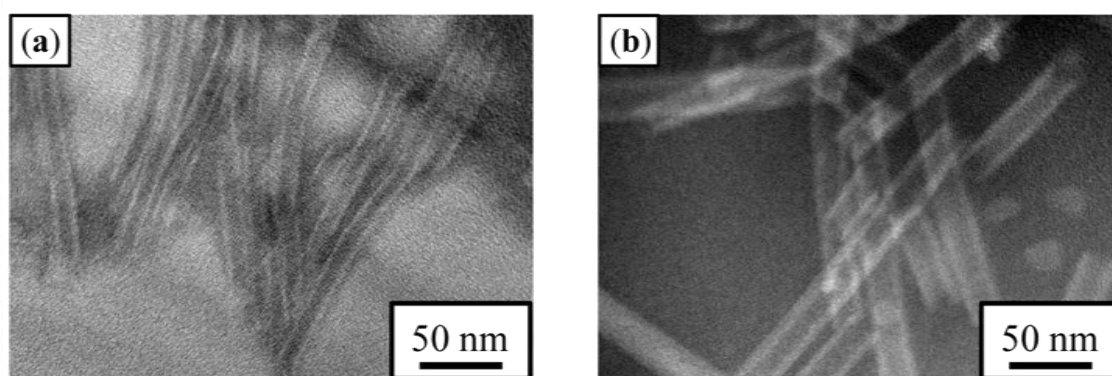


**Figure 1-1.** Negative-stained field emission-transmission electron microscopy (FE-TEM) images of (a) ONT-1 and (b) ONT-2.

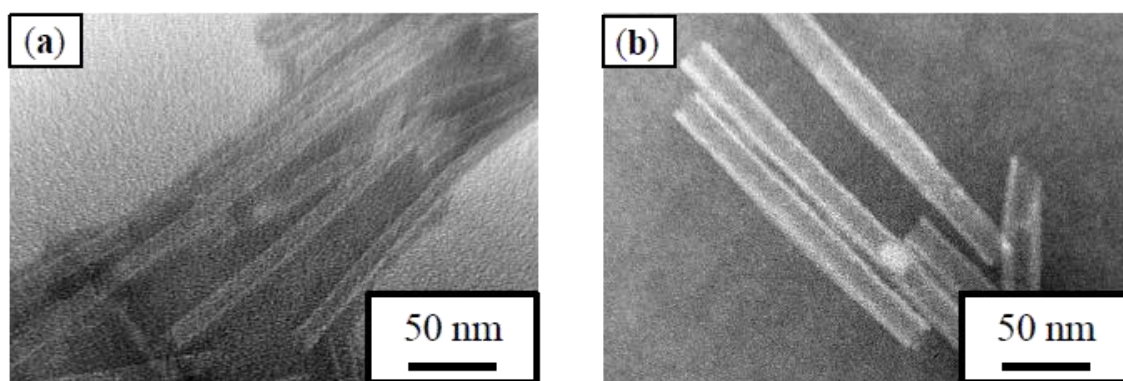


**Figure 1-2.** FE-TEM images of (a) ONT-1 evaporated from acetone and (b) ONT-2 evaporated from methanol.



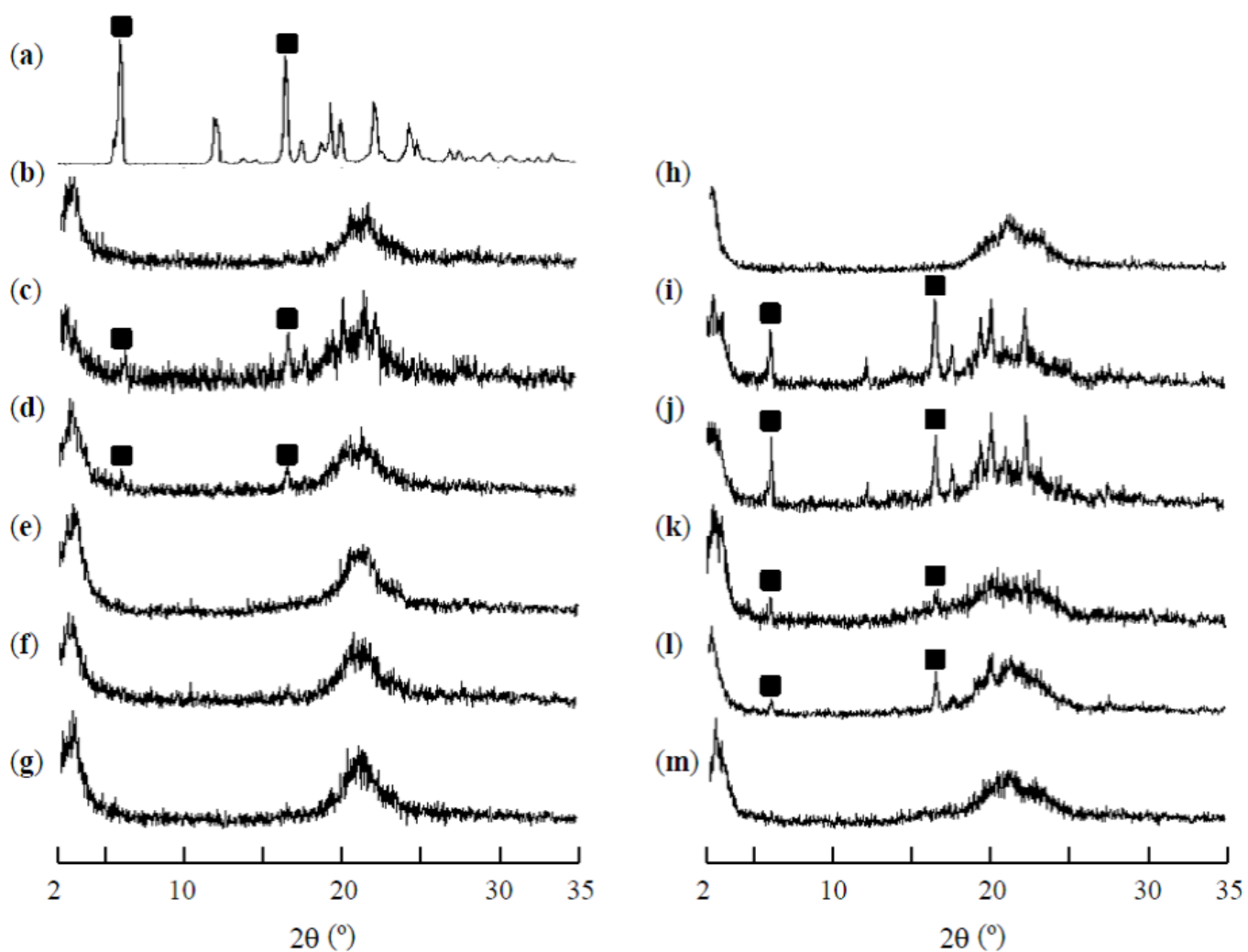


**Figure 1-3.** Powder X-ray diffraction (PXRD) patterns of (a) IBU crystal, (b) ONT-1, (c)-(g) IBU/ONT-1 EVPs at the drug contents of (c) 30 wt%, (d) 20 wt%, (e) 15 wt%, (f) 10 wt%, (g) 5 wt%, and (h) ONT-2, (i)-(m) IBU/ONT-2 EVPs at the drug contents of (i) 50 wt%, (j) 45 wt%, (k) 40 wt%, (l) 35 wt%, and (m) 30 wt%.

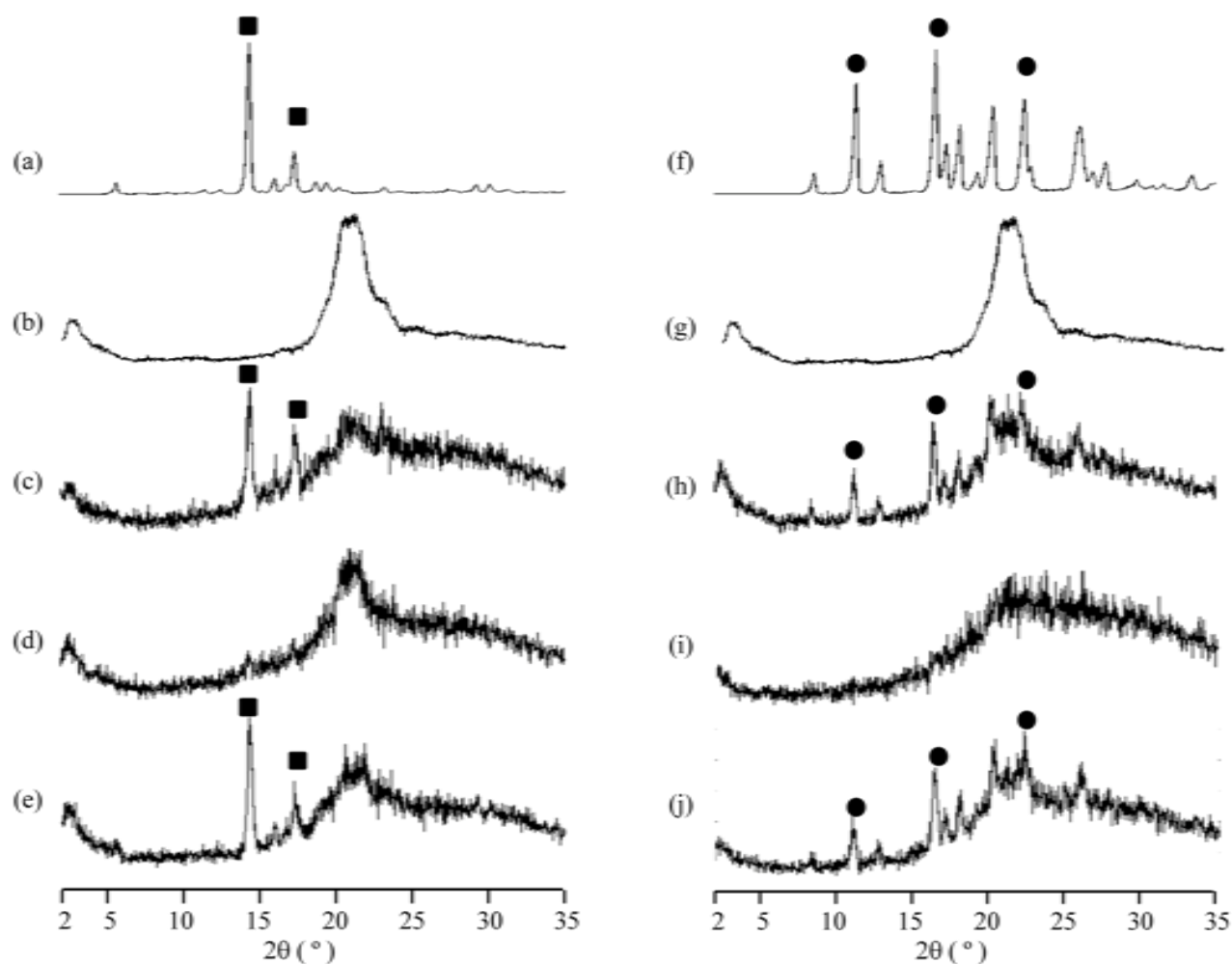


**Figure 1-4.** Powder X-ray diffraction (PXRD) patterns of HCT/ONT-1 and PHE/ONT-1 systems with various drug contents: (a) HCT, (b) ONT-1, (c) HCT/ONT-1 30 wt% physical mixture (PM), (d) HCT/ONT-1 30 wt% EVP, (e) HCT/ONT-1 50 wt% EVP, (f) PHE, (g) ONT-1, (h) PHE/ONT-1 30 wt% PM, (i) PHE/ONT-1 30 wt% EVP, and (j) PHE/ONT-1 50 wt% EVP. (■) HCT, (●) PHE.

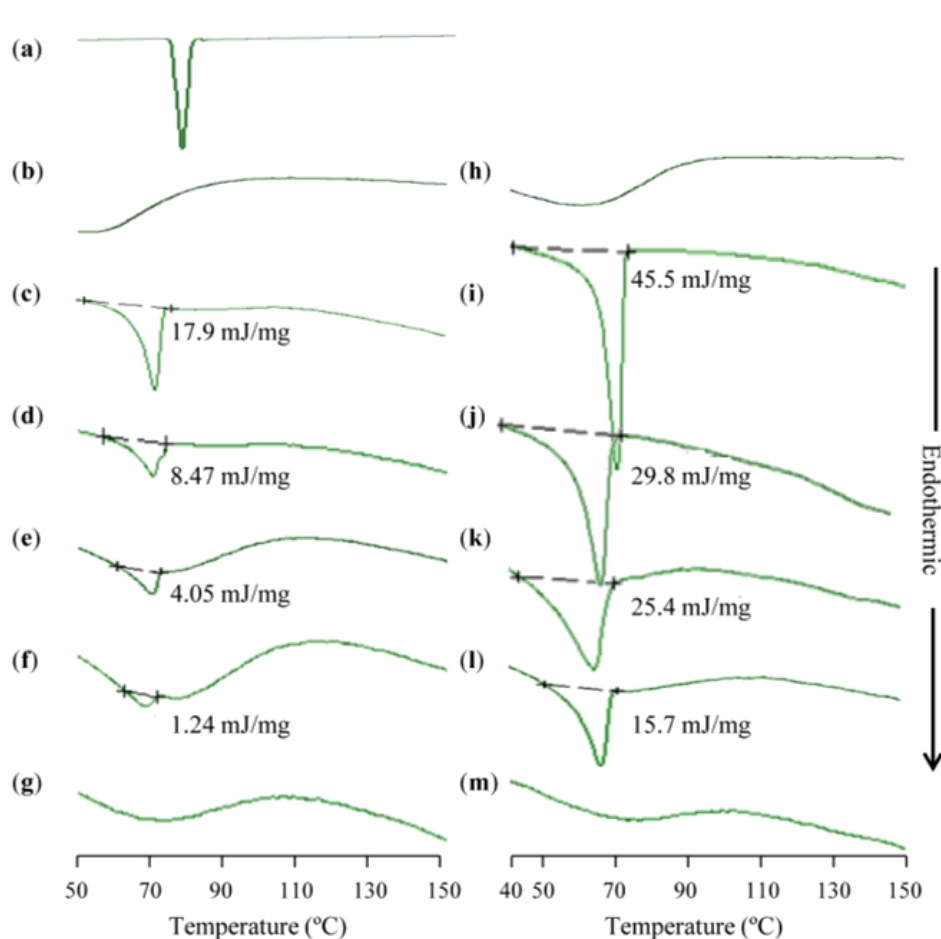


**Figure 1-5.** Differential scanning calorimetry (DSC) curves of (a) IBU crystal, (b) ONT-1, (c)-(g) IBU/ONT-1 EVPs at the drug contents of (c) 30 wt%, (d) 20 wt%, (e) 15 wt%, (f) 10 wt%, (g) 5 wt%, and (h) ONT-2, (i)-(m) IBU/ONT-2 EVPs at the drug contents of (i) 50 wt%, (j) 45 wt%, (k) 40 wt%, (l) 35 wt%, and (m) 30 wt%.

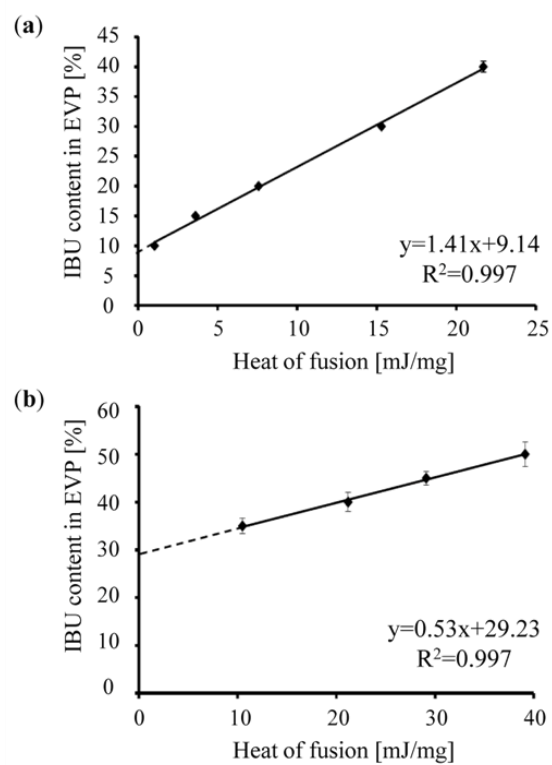


**Figure 1-6.** Plots of IBU content against the heat of fusion of IBU crystal melting calculated by the DSC curves of EVPs with (a) ONT-1 and (b) ONT-2.

## **PART II Evaluation of the molecular state of IBU-loaded ONT**

### **1. 2D $^1\text{H}$ - $^{13}\text{C}$ HETCOR spectroscopy for peak assignment**

The  $^1\text{H}$ - $^{13}\text{C}$  HETCOR measurements were performed to identify the  $^1\text{H}$  and  $^{13}\text{C}$  peaks in the spectra of IBU/ONT-1 EVP and IBU/ONT-2 EVP.<sup>30</sup> The reported  $^1\text{H}$  and  $^{13}\text{C}$  solid-state NMR spectra of IBU crystal and IBU encapsulated in mesoporous silica were used to support the peak assignment.<sup>31</sup>  $^1\text{H}$ - $^{13}\text{C}$  HETCOR spectra of IBU/ONT-1 EVP = 1 : 9 (weight ratio of IBU to ONT-1 in EVP) and IBU/ONT-2 EVP = 3 : 7 (weight ratio of IBU to ONT-2 in EVP) with different contact times are shown in Figure 2-1. A  $^1\text{H}$ - $^{13}\text{C}$  HETCOR spectrum with a short contact time allows for the detection of heteronuclear dipolar couplings between  $^1\text{H}$  and  $^{13}\text{C}$  atoms bound via covalent bonding. As shown in the spectra with the short contact time of 0.3 ms, all the  $^1\text{H}$  and  $^{13}\text{C}$  peaks in IBU were present. Furthermore, the glucose group and methylene chain of the ONT in IBU/ONT-1 EVP and IBU/ONT-2 EVP were also identified (Figure 2-1a, b). The more distant correlations between  $^1\text{H}$  and  $^{13}\text{C}$  were observed in the  $^1\text{H}$ - $^{13}\text{C}$  HETCOR spectra with contact times of 4 and 5 ms for IBU/ONT-1 and IBU/ONT-2 EVPs, respectively (Figure 2-1c, d).

### **2. 1D $^1\text{H}$ MAS NMR measurements**

High-resolution  $^1\text{H}$  NMR spectra was performed to evaluate the molecular state of

IBU and the ONTs in IBU/ONT EVPs (Figure 2-2). Crystalline IBU presented broad peaks characteristic ( $H_{2-3,10-13}$ ;  $H_{5,6,8,9}$ ;  $H_{14}$ ) of a rigid solid arising from the incomplete averaging of the strong homonuclear  $^1H$ - $^1H$  dipolar interaction in spite of the fast MAS conditions.<sup>30</sup> In contrast, the  $^1H$  MAS NMR spectra of encapsulated IBU samples, IBU/ONT-1 EVP and IBU/ONT-2 EVP present sharper aliphatic and aromatic lines even at low drug loadings (10 wt% for IBU/ONT-1 EVP and 30 wt% for IBU/ONT-2 EVPs). This sharpening of IBU  $^1H$  peaks has been previously observed when it is encapsulated in mesoporous MCM-41.<sup>32</sup> The homonuclear  $^1H$ - $^1H$  dipolar interactions were efficiently averaged by the rapid isotropic motion of IBU in the MCM-41 mesopores. Thus, the  $^1H$  spectra of IBU/ONT-1 EVP and IBU/ONT-2 EVP strongly indicated a rapid reorientation of mobile IBU in the ONTs. Meanwhile, it is worth noting that the peak corresponding to the IBU carboxyl proton was much broader in the EVPs than other peaks, and the peak broadening was accompanied by an upfield shift of IBU carboxyl proton compared with crystalline IBU. According to previous studies, the carboxyl proton of encapsulated IBU was involved in a chemical exchange reaction (intermediate exchange regime).<sup>33,34</sup> Thus, the carboxyl group of IBU could have been participating in an interaction with the ONT surface. The spectra of ONT-1 and ONT-2 both in pristine and EVPs showed much broader peaks, reflecting the lower mobility of

the ONTs. No significant difference was found between the ONT peaks in the pristine form and the EVPs. However, the peaks at 5–6 ppm in the spectrum of the pristine ONTs (indicated by arrows), which correspond to the hydroxyl proton of the glucose group on the outer surface of the ONTs, disappeared in the spectra of both EVPs.

### 3. 1D $^{13}\text{C}$ MAS NMR measurements

$^{13}\text{C}$  CP and SP spectra are shown in Figure 2-3, and the  $^{13}\text{C}$  chemical shifts are summarized in Tables 1 and 2. The peaks of the nuclei with low mobility are emphasized more in the  $^{13}\text{C}$  CP spectra, while those with high mobility are suppressed. On the other hand,  $^{13}\text{C}$  SP spectra reflect the nuclei independent of their mobility when the recycle delay is longer than the  $^{13}\text{C}$ -spin lattice relaxation time ( $T_1$ ). Only sharp peaks were found in the CP spectrum of crystalline IBU, reflecting the high degree of crystallinity (Figure 2-3a).<sup>35</sup> On the other hand, IBU in IBU/ONT-1 and IBU/ONT-2 EVPs showed two families of peaks corresponding to each  $^{13}\text{C}$  nucleus in the CP and/or SP spectra (Figure 2-3c-d, f-g), whose chemical shifts and peak shapes were very different from those of crystalline IBU. The two families of peaks were emphasized in either the CP or SP spectrum, indicating the IBU with either lower mobility or higher mobility. The dynamics of small guest drugs in host spaces is discussed by comparing  $^{13}\text{C}$  CP and SP spectra. IBU in mesopores has also been investigated in previous

articles.<sup>34,36</sup> The characteristic peaks enhanced in the SP spectrum were assigned to the IBU with extremely fast molecular motion, confined in the mesopores. In this study, the peaks emphasized in the SP spectrum (indicated in red font as “inner”) could belong to mobile IBU inside the hollow nanospace of ONT, since such highly mobile IBU should be inhabited with a certain hollow space formed by the ONT structure. On the other hand, the less mobile IBU emphasized in the CP spectrum could be ascribed to the less mobile IBU at the outer surface of ONT (indicated in blue font as “outer”).

### 3. Quantitative evaluation of loaded IBU in the inner and on the outer surface of ONT

The quantitative analysis of the encapsulation ratio of IBU inside the hollow nanospace against at the outer surface of both ONT-1 and ONT-2 was carried out using the SP spectrum (Figure 2-4). The integration ratio was estimated using the peak area of C<sub>3</sub> (“inner” and “outer”) after the process of the wave-form separation. The encapsulation ratio was determined to be 49.9 : 50.1 for IBU/ONT-1 EVP, and 65 : 35 for IBU/ONT-2 EVP. Namely, the encapsulation ratio of IBU in the hollow nanospace versus that on the outer surface can be considered approximately 1 : 1 for ONT-1 and 2 : 1 for ONT-2. Thus, the IBU was more efficiently encapsulated in the hollow nanospace than on the outer surface of ONT-2 for IBU/ONT-2 EVP, whereas for IBU/ONT-1 EVP, IBU encapsulation was equimolar between the inner hollow nanospace and the outer



surface of ONT-1. The difference in the encapsulated amounts could be explained by the different interaction strengths between IBU and the inner surfaces of the ONTs.

#### 4. Evaluation of the interaction between IBU and ONT

The changes in  $^{13}\text{C}$  peaks of IBU and the inner surface of both ONT-1 and ONT-2 are described as follows: The peak of the IBU carboxyl  $\text{C}_{1\text{ inner}}$  in IBU/ONT-1 and IBU/ONT-2 EVPs (Figure 2-5e, g) broadened and shifted to higher magnetic field at 178.7 and 180.3 ppm compared to the sharp melted IBU peak, which had a chemical shift of 181.3 ppm (Figure 2-5b). Fatnassi et al. reported that the peaks of IBU dimer and monomer were predicted to appear at 181.3 and 170.7 ppm, respectively.<sup>34</sup> Thus, the carboxyl carbon peak observed in the melted IBU likely derived from dimeric IBU, with no interaction with other additives. The chemical shift of  $\text{C}_{1\text{ inner}}$  should be due to the breakage of the IBU dimer structure, and subsequent interaction of the IBU monomer with ONT inner surface.<sup>34,37</sup> Moreover, the intensity of each IBU  $\text{C}_{\text{inner}}$  peak of IBU/ONT-1 and IBU/ONT-2 EVPs (Figure 2-3d, g) were compared with the melted IBU (Figure 2-6). Although all peaks of IBU in the inner nanospace of ONT were broaden compared with melted IBU, the peak broadening was strongest in the carboxyl group of IBU (Figure 2-3d, g), indicating that IBU interacted with ONT inner surface mainly through the carboxyl groups of IBU.<sup>38-40</sup> It has been reported that the changes in

chemical shift of  $^{13}\text{C}$  peaks between IBU dimer and monomer was around 7~10 ppm.<sup>34</sup>

Herein, the difference in chemical shift between the carboxyl group of the IBU interacted with the ONT inner surface and that of the melted IBU in dimeric structure was found to be not larger than 2 ppm. Thus, there could be a larger distribution of environments for the IBU carboxyl group, each with a different molecular mobility.<sup>32</sup> The exchange between the monomeric IBU bound to the inner surface and the freely mobile dimeric IBU inside the hollow nanospace of ONT could result in the broad averaged  $\text{C}_{1 \text{ inner}}$  peaks.

The number of resonances in the IBU aromatic groups was reduced in both IBU/ONT-1 and IBU/ONT-2 EVPs (Figure 2-3c-d, f-g) compared with those in the crystalline IBU (Figure 2-3a). The difference was likely due to a rapid tumbling of the IBU aromatic group both in the hollow nanospace and on the outer surface of ONTs, leading to an averaging of the resonance peaks.<sup>35</sup> On the other hand, the particular packing of the IBU molecules in the crystalline state resulted in crystallographic inequivalence.<sup>41</sup> The  $\text{C}_{12}$  and  $\text{C}_{13}$  peaks of crystalline IBU were averaged to a single, sharp  $\text{C}_{12, 13 \text{ inner}}$  peak whose intensity was enhanced in the SP spectrum compared to the CP spectrum in both the IBU/ONT-1 and IBU/ONT-2 EVPs. The single sharp peak of IBU  $\text{C}_{12, 13 \text{ inner}}$  in ONTs was similar to that of encapsulated IBU in mesoporous

MCM-41.<sup>33</sup> Moreover, the broad peaks observed at the foot of the sharp C<sub>12,13</sub> peak could belong to C<sub>12</sub> and C<sub>13</sub> on the outer surface of ONTs. In order to characterize the interactions between IBU and the ONT inner surface, the changes in the host ONTs peaks due to encapsulation of IBU were investigated. IBU loading did not show any significant changes in chemical shift or peak shape of the inner surface of ONT-1 (Figure 2-7a, b). In contrast to ONT-1, the ONT-2 in the EVP showed drastic changes compared to the pristine form (Figure 2-7c, d). The C<sub>47''</sub> peak on the inner surface of ONT-2 showed a chemical shift from 175.6 ppm to 172.5 ppm in IBU/ONT-2 EVP, as assigned by the 2D <sup>1</sup>H-<sup>13</sup>C HETCOR spectrum in Figure 2-8. Furthermore, the C<sub>49''</sub> peak derived from the inner surface of ONT-2 in the IBU/ONT-2 EVP showed a change in peak shape with respect to ONT-2 (Figure 2-9). These changes could be due to the interactions between IBU and ONT-2 at the inner surface. The inner surface of ONT-2 showed larger peak changes than those in ONT-1, which indicated the stronger interactions between IBU and inner surface of ONT-2 compared to ONT-1.

The interaction between IBU and ONT outer surface was discussed. The peak of the IBU C<sub>1 outer</sub> in both IBU/ONT-1 and IBU/ONT-2 EVPs (Figure 2-5d, f) broadened and shifted to higher magnetic field at 178.8 and 179.2 ppm, respectively, compared to the sharp melted IBU peak, in a manner similar to that observed in the inner nanospace of

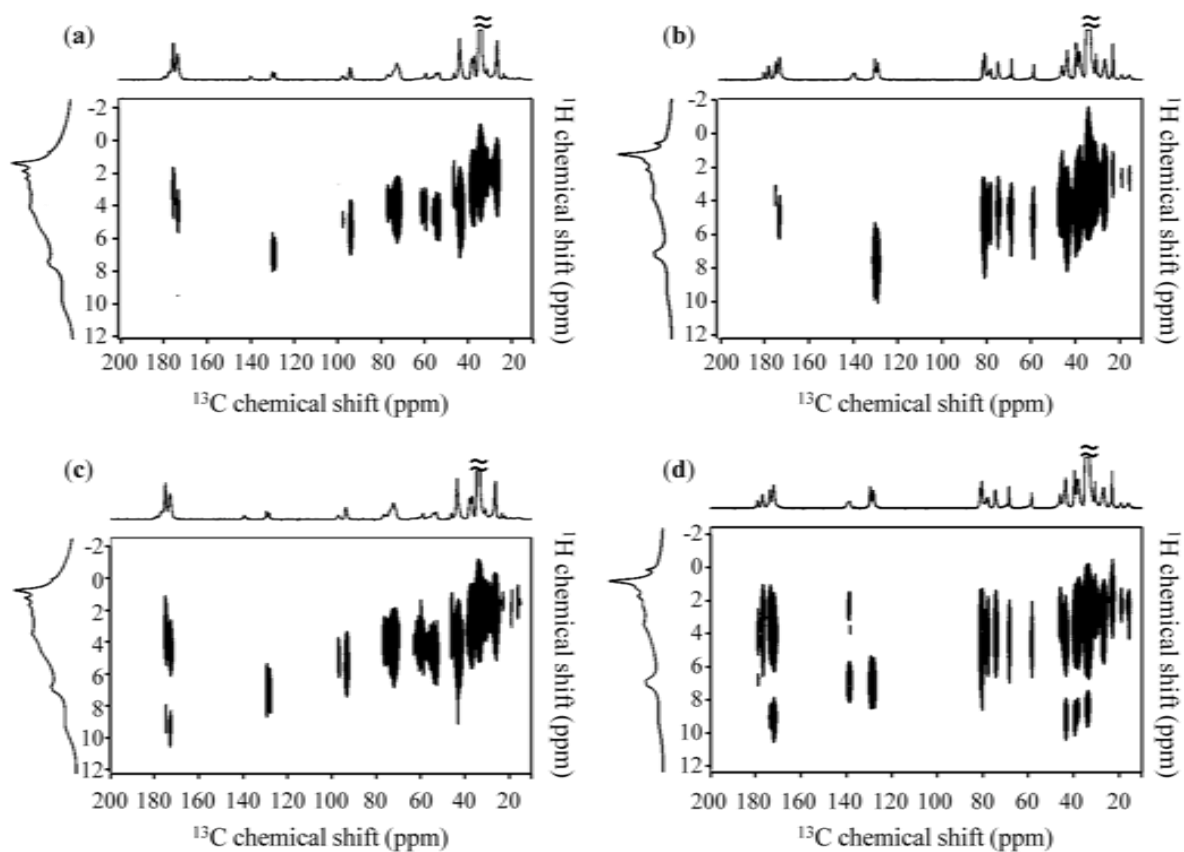
ONTs (Figure 2-5b). It has been also reported that the IBU carboxyl carbon in an amorphous solid dispersion with polyvinylpyrrolidone shifted to a higher magnetic field at 178.3 ppm due to the formation of hydrogen bonds between the carboxyl group of IBU and the carbonyl group of polyvinylpyrrolidone.<sup>42</sup> Here, the peak shift of  $C_{1\text{ outer}}$  to a higher magnetic field can be attributed to intermolecular interactions between the carboxyl group of monomeric IBU with the hydroxyl group on the glucose of the ONT outer surface. The peaks of ONT outer surface groups were compared with those of IBU/ONT EVPs (Figure 2-10). Changes in the shape of peaks derived from the glucose group on the outer surface of both the ONTs were observed, particularly the  $C_{4', 6', 13'}$  for ONT-1, and the  $C_{2'', 6'', 13''}$  for ONT-2. It was confirmed that IBU interacted with the glucose hydroxyl group of both ONT-1 and ONT-2 at the outer surface. Here, the two peaks of  $C_{2'}$  in ONT-1 were assigned to the  $\alpha$ -anomer (93.3 ppm) and  $\beta$ -anomer (96.4 ppm) of the glucose (Figure 2-10a),<sup>44</sup> indicating a mixture of the  $\alpha$ - and  $\beta$ -anomers in ONT-1. This information also provide a reasonable explanation for the  $C_{3\text{ outer}}$  peak of IBU in IBU/ONT-1 EVP appearing as two peaks in Figure 2-4a. The carboxyl group next to  $C_3$  in the chemical structure of IBU should interact with the hydroxyl group in either the  $\alpha$ - or  $\beta$ -anomer of ONT-1 glucose at the outer surface. Furthermore, the interactions between IBU and the outer surfaces of the ONTs were evaluated by using

$^1\text{H}$ - $^{13}\text{C}$  HETCOR spectroscopy with a longer contact time (Figure 2-1c, d). The HETCOR spectra clearly showed well-separated cross peaks in both the IBU/ONT-1 and IBU/ONT-2 EVPs (indicated by the dotted lines in Figure 2-11). These correlations arose from an interaction between the less mobile  $\text{C}_{1\text{ outer}}$  of IBU and the hydroxyl proton from the glucose group on the outer surface of the ONTs. As such, this result confirmed that the peaks denoted “outer” belonged to the IBU at the outer surface of the ONTs.

Figure 2-12 shows schematic illustrations of both the IBU/ONT EVPs. As shown in FE-SEM images of the IBU/ONT EVPs, ONT fibers existed in a network, and individual fibers showed widths of 30–60 nm, while the diameters of both ONT-1 and ONT-2 was ca. 14–16 nm as shown in the FE-TEM images (Figure 1-1). It has been reported that tubular structures that possess high aspect ratios and flexibilities, such as carbon nanotubes and ONTs, have a high probability of entanglement and close packing with each other.<sup>18,44</sup> Thus, the ONTs used in this study could form bundles, and in the EVPs these bundles were randomly arranged and aggregated with each other. There are two types of spaces where IBU could be loaded: either the hollow nanospace of an ONT, or on the outer surface of ONTs. In both the IBU/ONT-1 and IBU/ONT-2 EVPs, the IBU in the inner nanospace had much higher mobility, while IBU existed at the outer

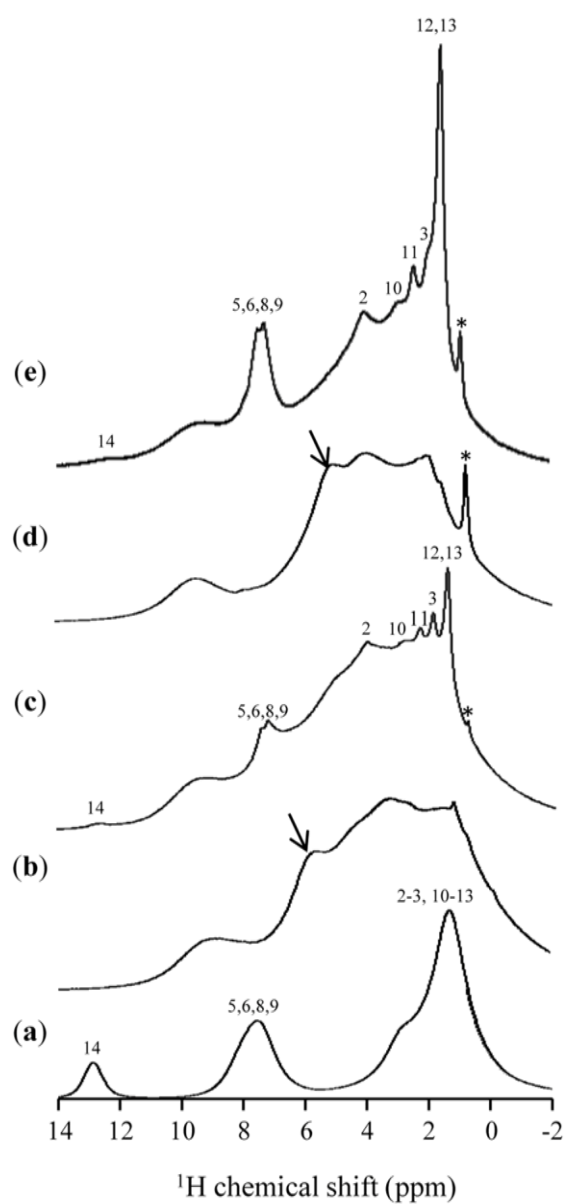
surface of the ONT was less mobile. Meanwhile, the IBU in the inner hollow nanospace had much higher mobility, exhibiting isotropic motion, and there was exchange between the monomeric IBU bound to the inner surface and the dimeric IBU that was freely mobile in the hollow nanospace. The maximum amounts of IBU encapsulation for ONT-1 and ONT-2 were ca. 10 wt% and 30 wt%, respectively. The encapsulation ratio for IBU at the inner hollow nanospace versus at the outer surface was about 1 : 1 for IBU/ONT-1 EVP, and 2 : 1 for IBU/ONT-2 EVP. Thus, the amounts of IBU associated with the inner hollow nanospace and outer surface in ONT-1 were calculated to be 5 wt% and 5 wt%, while in ONT-2 those were 20 wt% and 10 wt%, respectively. The IBU in the inner hollow nanospace of ONT-1 was weakly held via interactions between the carboxyl group of IBU and the inner surface. In contrast, those in IBU/ONT-2 EVP were strongly held in the inner hollow nanospace through electrostatic interactions of the IBU carboxyl group with the amino group on the inner surface of ONT-2. This stronger interaction could result in encapsulation of a larger amount of IBU into ONT-2 than that into ONT-1. At the outer surface, weak interaction was formed between the IBU carboxyl group and the ONT glucose group for both IBU/ONT-1 and IBU/ONT-2 EVPs. Comparing the ONT-1 and ONT-2 EVPs, ONT-2 showed approximately three times greater IBU encapsulation than ONT-1. The difference in the amounts

encapsulated by ONT-1 and ONT-2 could be explained by the different interaction strengths between IBU and the inner surfaces of the ONTs. IBU is a propionic acid with a pKa of 4.4~5.4.<sup>45</sup> ONT-1 had an anionic inner surface of carboxyl groups, while ONT-2 had a cationic inner surface of amino groups. The amino group on the inner surface of the cationic ONT-2 could retain higher amounts of IBU via electrostatic interactions with the carboxyl group during the evaporation process. On the other hand, the smaller amount of IBU encapsulated within ONT-1 could be due to the presence of a carboxyl group on the anionic ONT-1 inner surface, which could repel the IBU. The maximum encapsulation of neutral drugs (HCT and PHE) within ONT-1 was about 30 wt% (Figure 1-4), similar to the IBU maximum amount loaded into ONT-2 (Figure 1-3). This result supported the fact that the drug encapsulation efficacy strongly depends on the interaction mode between the drug and the inner and outer surfaces of the ONT.

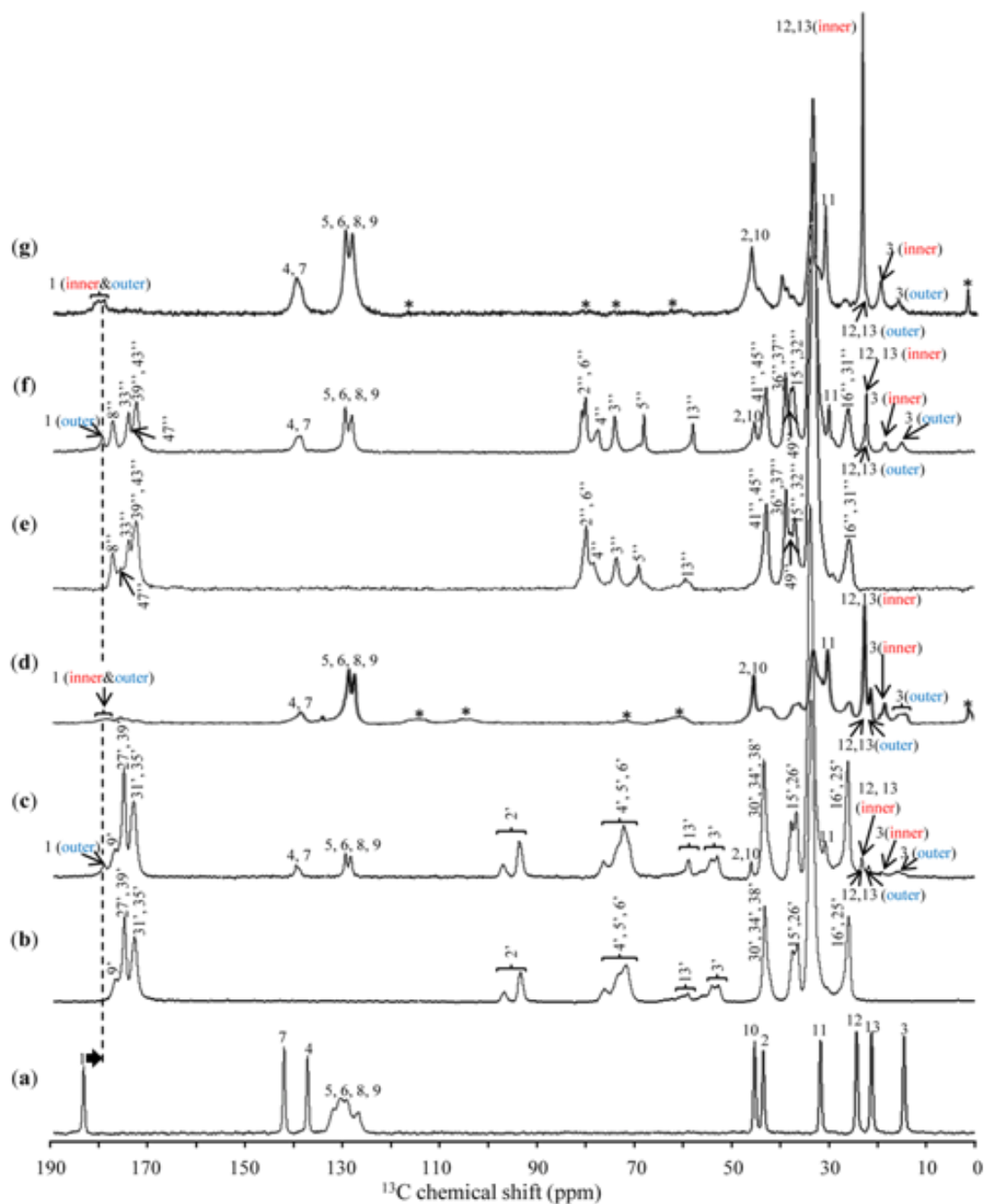


**Figure 2-1.** 2D  $^1\text{H}$ - $^{13}\text{C}$  heteronuclear correlation (HETCOR) spectra of (a) IBU/ONT-1 = 1 : 9 EVP (contact time = 0.3 ms), (b) IBU/ONT-2 = 3 : 7 EVP (contact time = 0.3 ms), (c) IBU/ONT-1 = 1 : 9 EVP (contact time = 4 ms), and (d) IBU/ONT-2 = 3 : 7 EVP (contact time = 5 ms).





**Figure 2-2.** 1D  $^1\text{H}$  NMR spectra ( $\nu_{\text{MAS}} = 40$  kHz) of (a) IBU crystal, (b) ONT-1, (c) IBU/ONT-1 = 1 : 9 EVP, (d) ONT-2, and (e) IBU/ONT-2 = 3 : 7 EVP. The asterisks represent the peak of the impurity in each ONT, and the arrows represent the peak of hydroxyl group in glucose group of ONT.



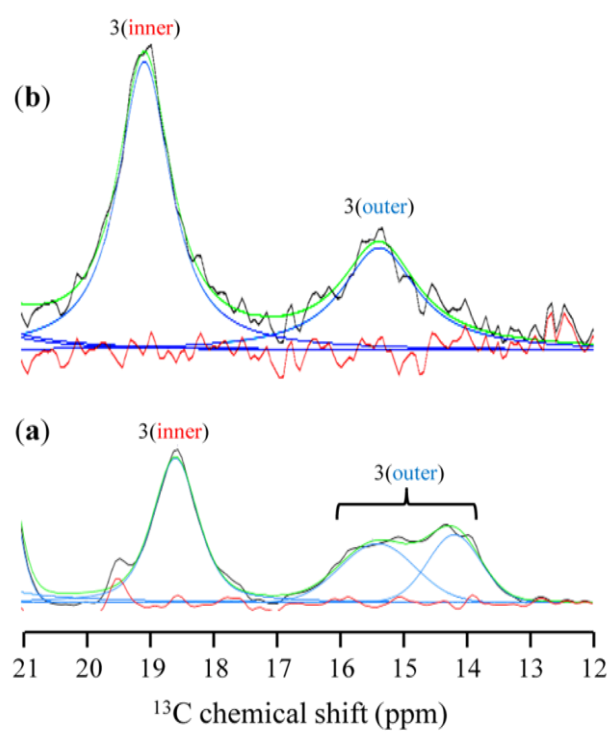
**Figure 2-3.** 1D  $^{13}\text{C}$  NMR spectra ( $\nu_{\text{MAS}} = 40$  kHz) of (a) crystalline IBU (CP), (b) ONT-1 (CP), (c) IBU/ONT-1 = 1:9 EVP (CP), (d) IBU/ONT-1 = 1:9 EVP (SP), (e) ONT-2 (CP), (f) IBU/ONT-2 = 3:7 EVP (CP), and (g) IBU/ONT-2 = 3:7 EVP (SP). The asterisks represent the impurity peak in each ONT.

Table 1.  $^{13}\text{C}$  CP chemical shift of IBU, ONT-1, ONT-2, and in IBU/ONT EVPs.

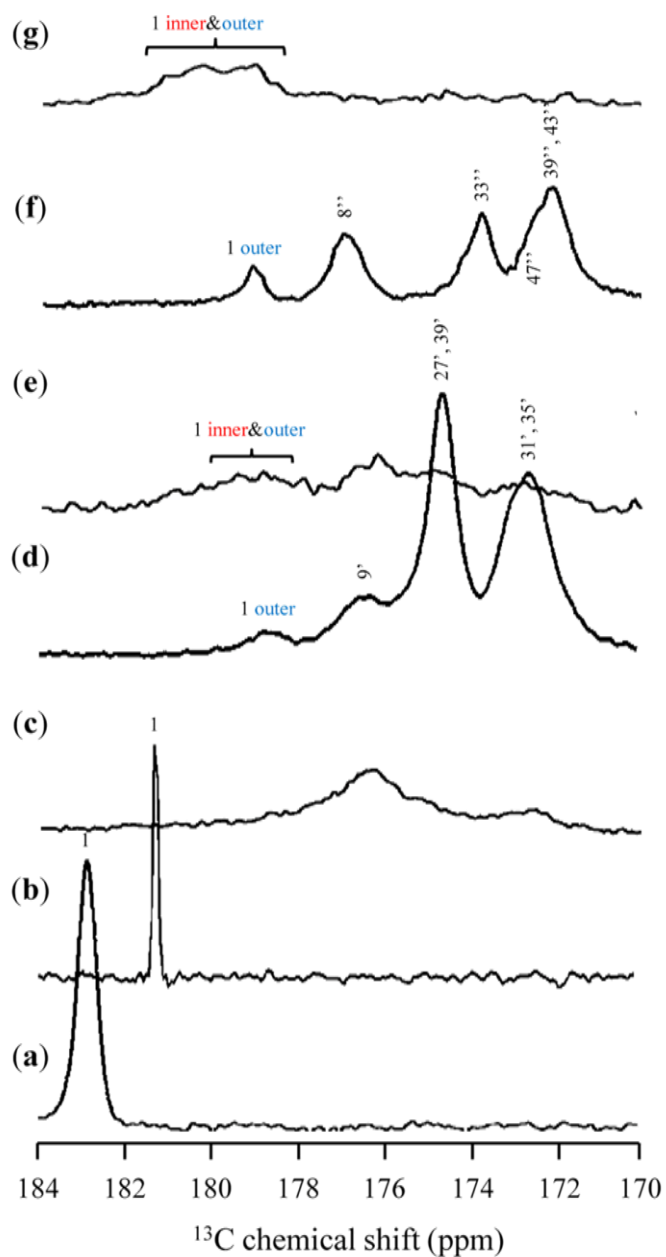
Assignment	<sup>13</sup> C CP chemical shift (ppm)			
	Intact	IBU/ONT-1 EVP	IBU/ONT-2 EVP	
IBU	C1	183.0	178.8 (outer)	179.2 (outer)
	C3	15.3	18.7 (inner)	19.0 (inner)
		137.2 (C4)	15.8/14.3 (outer)	15.7 (outer)
	C4,7	142.0 (C7)	139.2	139.0
	C5,6,8,9	126.8-132.1	128.0, 129.1	128.1, 129.4
	C2,10	44.1 (C2)	45.6	45.8
		45.8 (C10)		
	C11	32.4	30.4	30.5
C12,13	24.9 (C12)	22.8 (inner)	22.9 (inner&outer)	
	21.9 (C13)	22.8, 21.6 (outer)		
ONT-1	C2'	93.3 (α-anomer)	93.3 (α-anomer)	
		96.5 (β-anomer)	96.4 (β-anomer)	
	C3'	52.5, 54.0	52.6, 54.0	
	C4'-6'	71.5-75.9	71.9-76.1	
	C9'	176.6	176.3	
	C13'	58.9	58.4	
	C15',26'	36.3, 37.3	36.4, 37.4	
	C16',25'	25.8	25.8	
	C27',39'	174.6	174.6	
	C31',35'	43.0	172.7	
C30'-38'	172.5	43.0		
ONT-2	C2'',6''	80.2		80.4, 81.0
	C3''	74.0		74.4
	C4''	78.7		78.2
	C5''	69.5		68.4
	C8''	177.2		177.0
	C13''	59.1		58.4
	C15'',32''	37.6		37.9
	C16'',31''	26.5		26.6
	C33''	173.8		173.7
	C36'',37''	39.4		39.4
	C39'',43''	172.3		172.1
	C41'',45''	43.4		43.4
	C47''	175.6		172.5
	C49''	38.5		38.4

Table 2.  $^{13}\text{C}$  SP chemical shift of IBU in IBU/ONT EVPs.

Assignment		<sup>13</sup> C SP chemical shift (ppm)	
		IBU/ONT-1 EVP	IBU/ONT-2 EVP
IBU	C1	178.7 (inner & outer)	180.3 (inner) 179.0 (outer)
	C3	18.5 (inner) 15.1/14.3 (outer)	19.0 (inner) 15.3 (outer)
	C4,7	138.8	139.5
	C5,6,8,9	127.9, 129.1	128.0, 129.3
	C2,10	45.6	45.7
	C11	30.4	30.4
	C12,13	22.7 (inner) 22.7, 21.5 (outer)	22.8 (inner & outer)



**Figure 2-4.** Wave-form separation of  $^{13}\text{C}$  SP NMR spectra ( $\nu_{\text{MAS}} = 40$  kHz) for (a) IBU/ONT-1 = 1 : 9 EVP and (b) IBU/ONT-2 = 3 : 7 EVP from 12 ppm to 21 ppm.



**Figure 2-5.** 1D  $^{13}\text{C}$  NMR spectra ( $\nu_{\text{MAS}} = 40$  kHz) spectra of (a) IBU crystal (CP), (b) melted IBU measured at 70 °C (SP), (c) ONT-1 (SP), (d) IBU/ONT-1 = 1 : 9 EVP (CP), (e) IBU/ONT-1 = 1 : 9 EVP (SP), (f) IBU/ONT-2 = 3 : 7 EVP (CP), and (g) IBU/ONT-2 = 3 : 7 EVP (SP) from 170 ppm to 184 ppm.

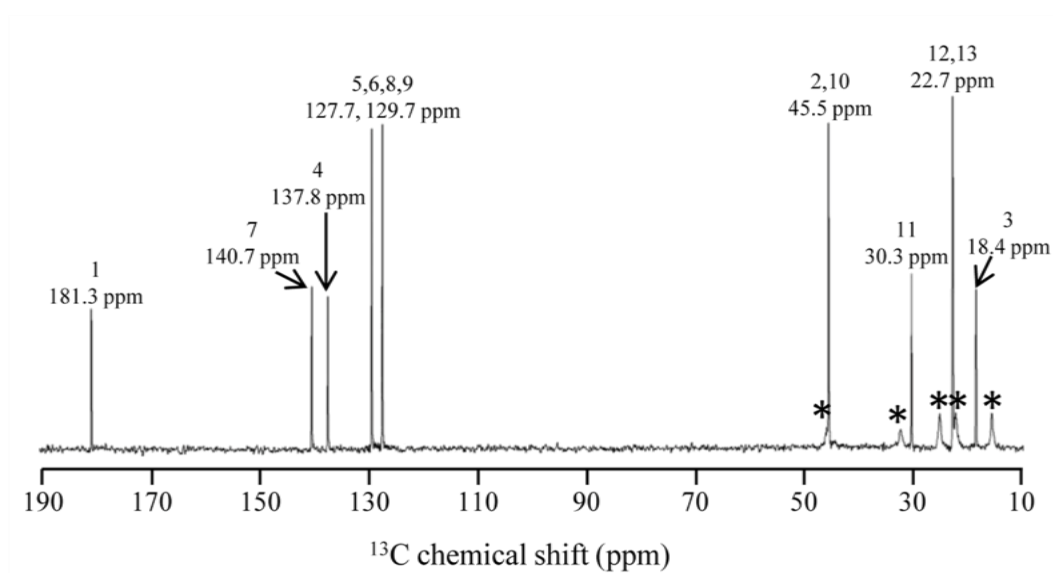


**Figure 2-6.**  $^{13}\text{C}$  SP spectrum ( $\nu_{\text{MAS}} = 40$  kHz) of melted IBU at 70 °C from 10–190 ppm. Asterisks indicate peaks of remaining crystalline IBU.

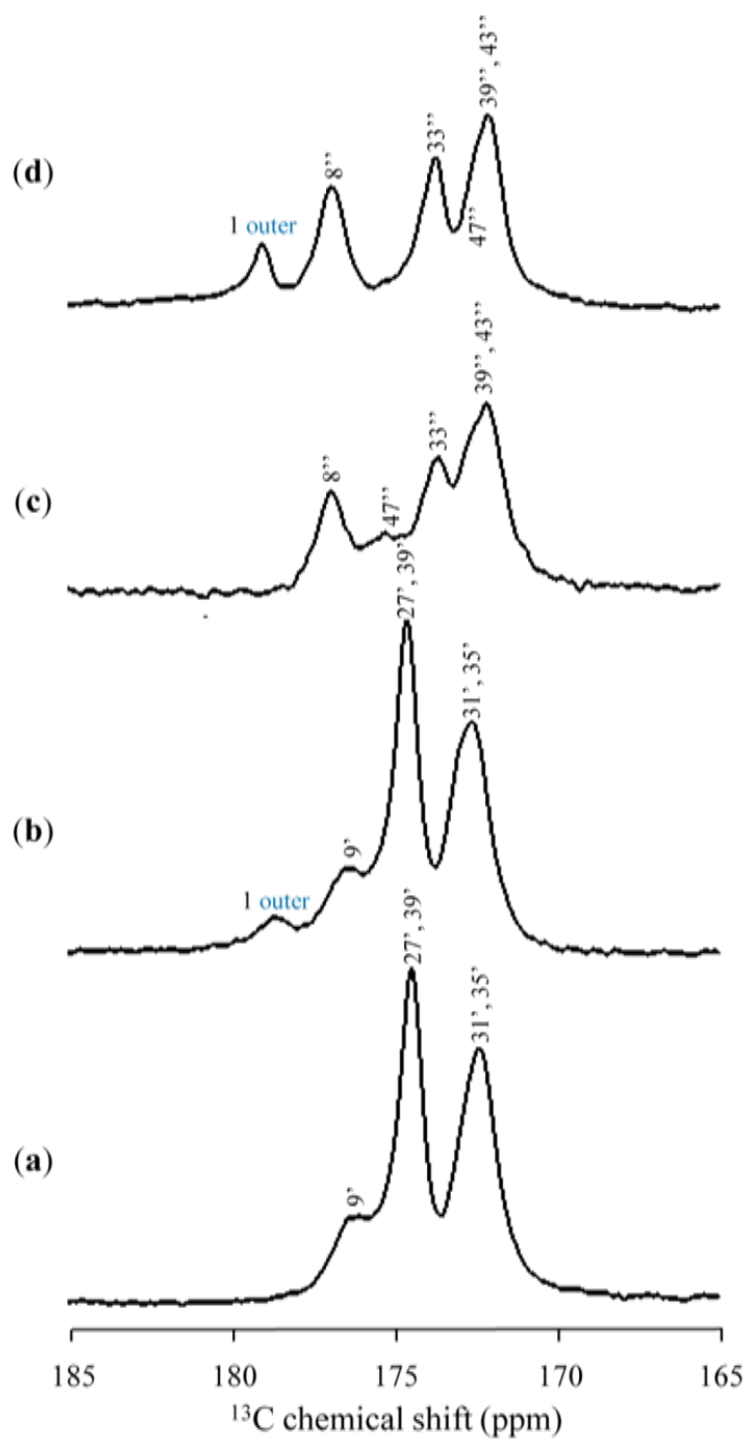


**Figure 2-7.** 1D  $^{13}\text{C}$  CP NMR spectra ( $\nu_{\text{MAS}} = 40$  kHz) spectra of (a) ONT-1, (b) IBU/ONT-1 = 1:9 EVP, (c) ONT-2, and (d) IBU/ONT-2 = 3:7 EVP from 165 –185 ppm.



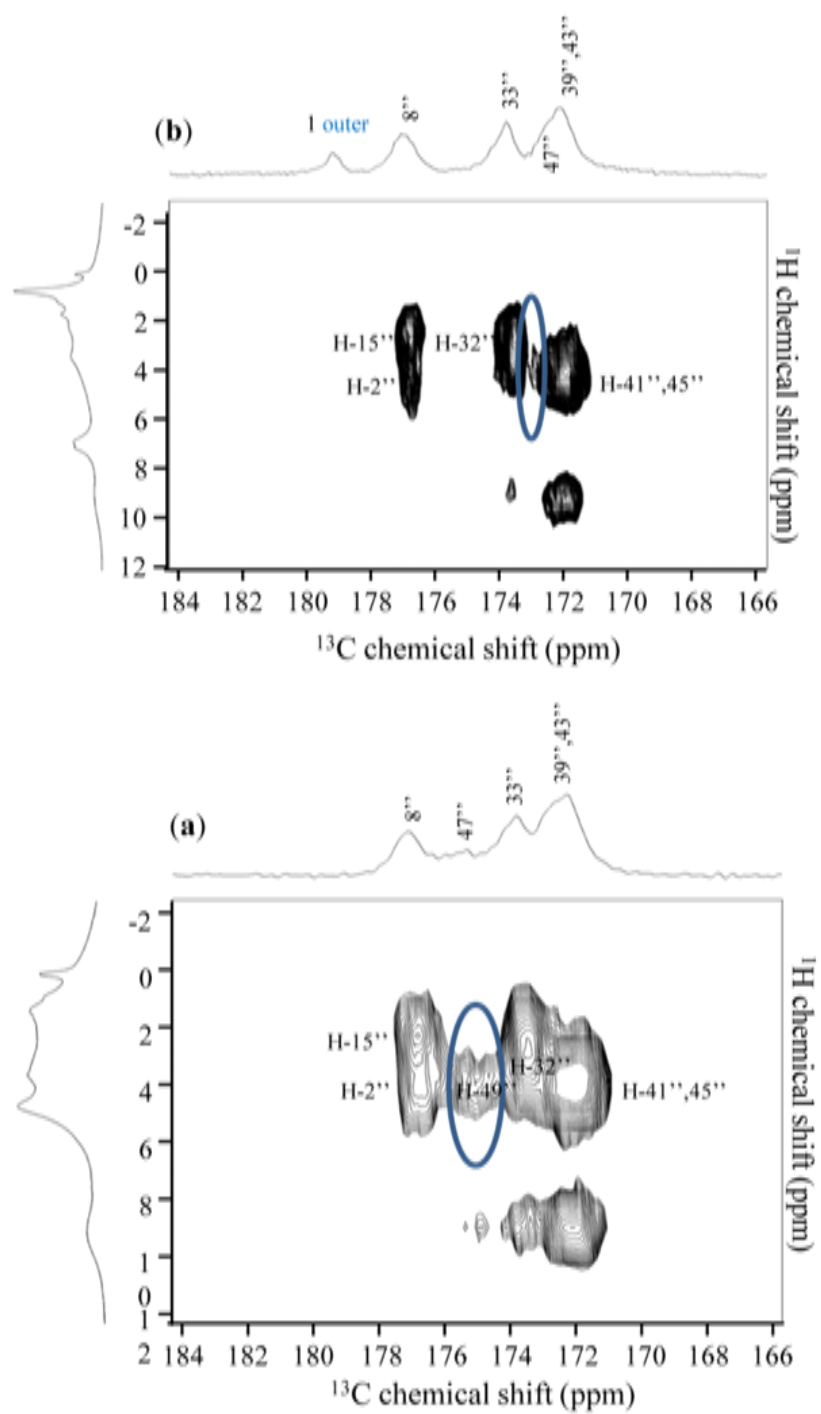


**Figure 2-8.** 2D  $^1\text{H}$ - $^{13}\text{C}$  heteronuclear correlation (HETCOR) spectra of (a) ONT-2 and (b) IBU/ONT-2 = 3:7 EVP.

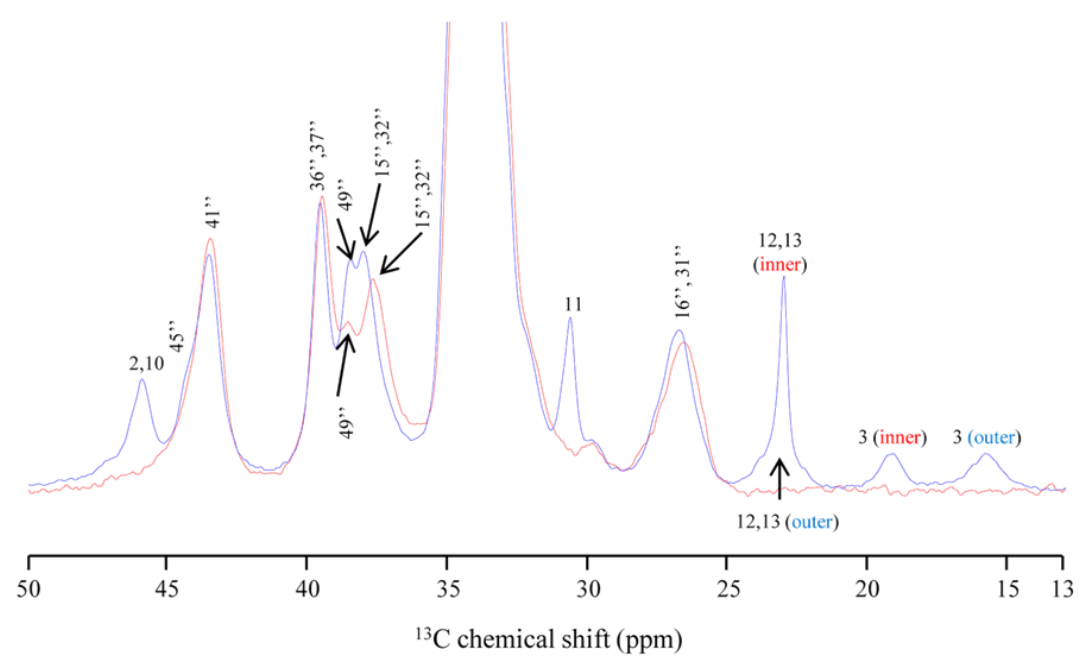


**Figure 2-9.** 1D  $^{13}\text{C}$  CP NMR spectra ( $\nu_{\text{MAS}} = 40$  kHz) spectra of ONT-2 (red line), and IBU/ONT-2 = 3:7 EVP (blue line) from 13–50 ppm.

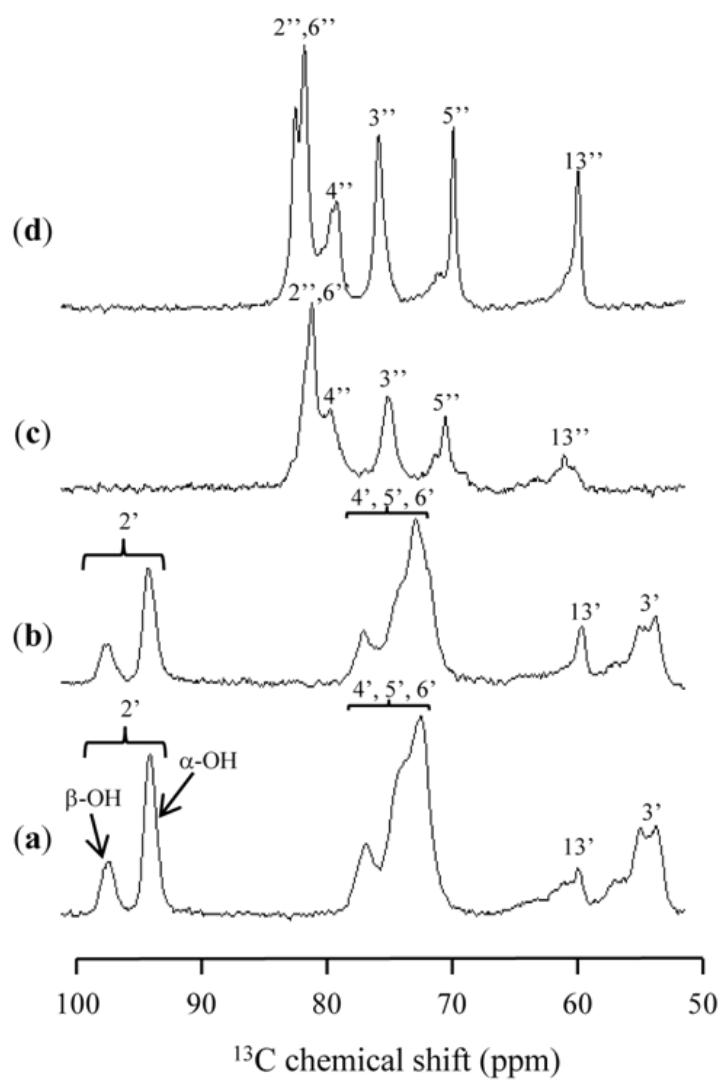


**Figure 2-10.** 1D  $^{13}\text{C}$  CP NMR spectra ( $\nu_{\text{MAS}} = 40$  kHz) spectra of (a) ONT-1, (b) IBU/ONT-1 = 1:9 EVP, (c) ONT-2, and (d) IBU/ONT-2 = 3:7 EVP from 50–100 ppm.

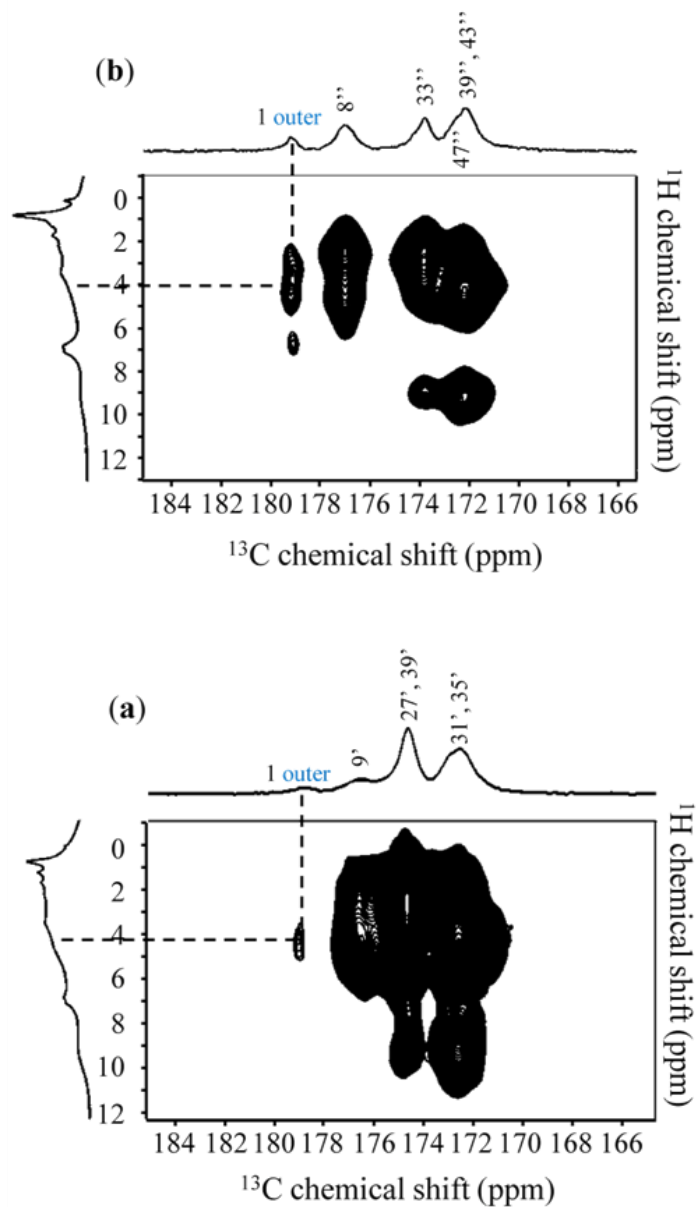


**Figure 2-11.** 2D  $^1\text{H}$ - $^{13}\text{C}$  heteronuclear correlation (HETCOR) spectra of (a) IBU/ONT-1 = 1 : 9 EVP (contact time = 4 ms) and (b) IBU/ONT-2 = 3 : 7 EVP (contact time = 5 ms).

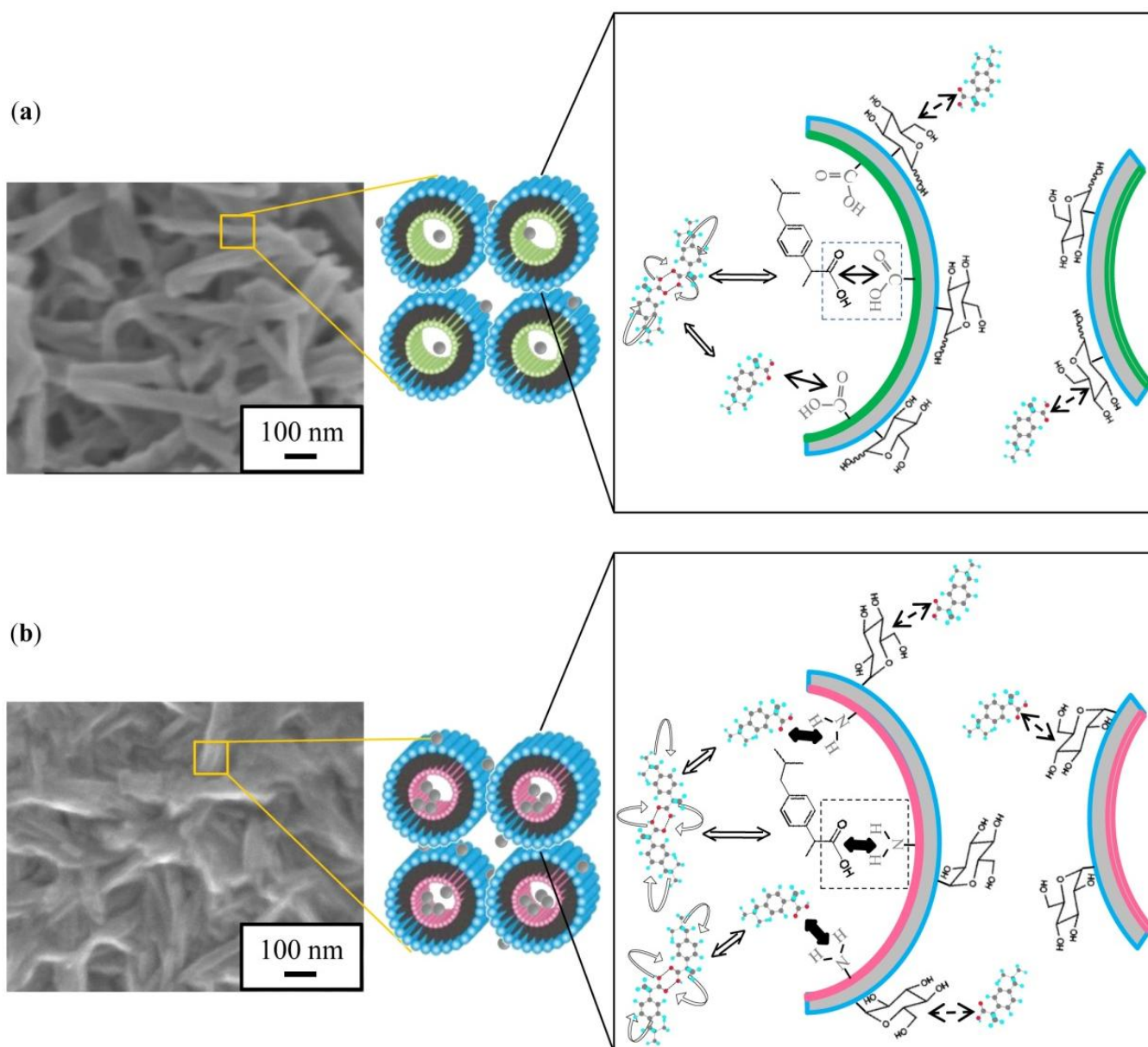


**Figure 2-12.** Field emission-scanning electron microscopy (FE-SEM) images (left) and schematic illustrations (right) of (a) IBU/ONT-1 = 1:9 EVP and (b) IBU/ONT-2 = 3:7 EVP.  $\longleftrightarrow$ : strong interaction (inner surface);  $\longleftrightarrow$ : weak interaction (inner surface);  $\longleftrightarrow$ : weak interaction (outer surface);  $\longrightarrow$ : high rotation;  $\longleftrightarrow$ : exchange.

### **PART III    Dissolution characteristics of IBU from each ONT**

Dissolution properties of IBU from ONT-1 and ONT-2 in acetate buffer solution (pH 4.0, 37°C) were investigated. The IBU dissolution profiles from crystalline IBU, IBU/ONT-1 = 1 : 9 EVP and IBU/ONT-2 = 3 : 7 EVP are represented in Figure 3-1. The IBU/ONT-1 = 1 : 9 EVP exhibited much fast dissolution from the initial stage of dissolution profile. The concentration of dissolved IBU from IBU/ONT-1 EVP at sampling times of 5 min accumulated to 7.0 µg/mL, much higher than that of crystalline IBU of 2.7 µg/mL. The dissolution improvement could be largely attributed to amorphization of IBU. The dissolution behavior coincide with the result that amorphous HCT and PHE encapsulated in ONT-1 showed rapid dissolution (Figure 3-2).<sup>27</sup> On the contrary, the dissolution profile of IBU from IBU/ONT-2 = 3 : 7 EVP sample was significantly different. The IBU concentration reached to 2.3 µg/mL at 5 min, due to the initial burst dissolution of IBU. Then, the rest of IBU followed a typical sustained dissolution and dissolved slowly than crystalline IBU. The difference in IBU dissolution behavior between IBU/ONT-1 EVP and IBU/ONT-2 EVP could be attributed to the different interaction with functional groups of ONT inner and outer surface.

Dissolution of IBU from the ONTs shows three identifiable stages (Figure 3-3).<sup>44</sup> Firstly, water molecules penetrate into both the inner hollow nanospace and the

interstitial spaces between the ONTs, causing the ONTs to separate from the bundles. The second process is the diffusion of ONTs into the dissolution medium, accompanied by the release of IBU from the interstitial space. The final stage is the release of IBU from the inner hollow nanospace. When the IBU/ONT-1 EVP was dispersed in a dissolution medium, IBU at the outer surface was immediately released, and the IBU inside the hollow nanospace rapidly diffused out. The interaction between IBU and the inner surface of anionic ONT-1 was so weak that IBU was difficult to retain within the hollow nanospace. On the other hand, the IBU/ONT-2 EVP showed two-step IBU dissolution. The burst release of IBU from ONT-2 over the first 5 min could be mainly attributed to the release of IBU from the outer surface of ONT-2. The slow dissolution of IBU after this step was due to the release of the remaining IBU from the inner hollow nanospace, which was slowed by the strong electrostatic interactions between IBU and the inner surface of cationic ONT-2.

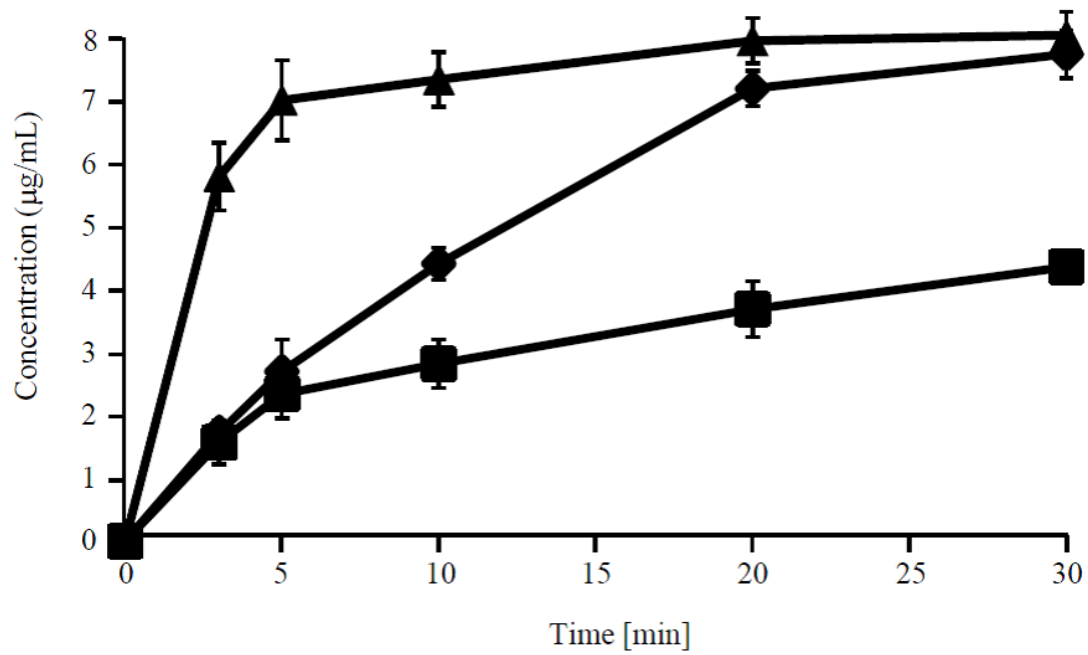


**Figure 3-1.** Dissolution profiles of (▲) IBU/ONT-1 = 1 : 9 EVP, (◆) IBU crystal, and (■) IBU/ONT-2 = 3 : 7 EVP in acetate buffer solution at pH 4.0, 37 °C ( n = 3, mean  $\pm$  S.D.).



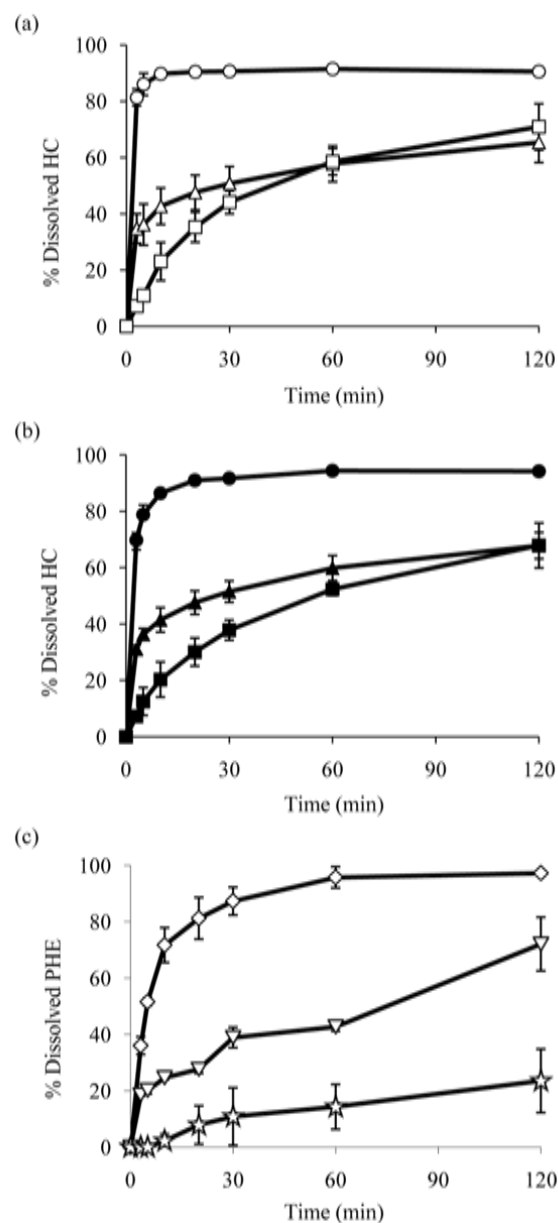


**Figure 3-2.** Dissolution profiles of HCT/ONT-1 and PHE/ONT-1 systems using a dissolution test apparatus according to the Japanese Pharmacopeia (JP) XVI paddle method at 37 °C. ( n = 3, mean  $\pm$  S.D.) (a) HCT/ONT-1 system in JP 2<sup>nd</sup> fluid (pH 6.8); (□) HCT, (△) HCT/ONT-1 30 wt% PM, and (○) HCT/ONT-1 30 wt% EVP, (b) HCT/ONT-1 system in JP 1<sup>st</sup> fluid (pH 1.2); (■) HCT, (▲) HCT/ONT-1 30 wt% PM, and (●) HCT/ONT-1 30 wt% EVP, and (c) PHE/ONT-1 system in JP 2<sup>nd</sup> fluid (pH 6.8); (☆) PHE, (▽) PHE/ONT-1 30 wt% PM, and (◇) PHE/ONT-1 30 wt% EVP.

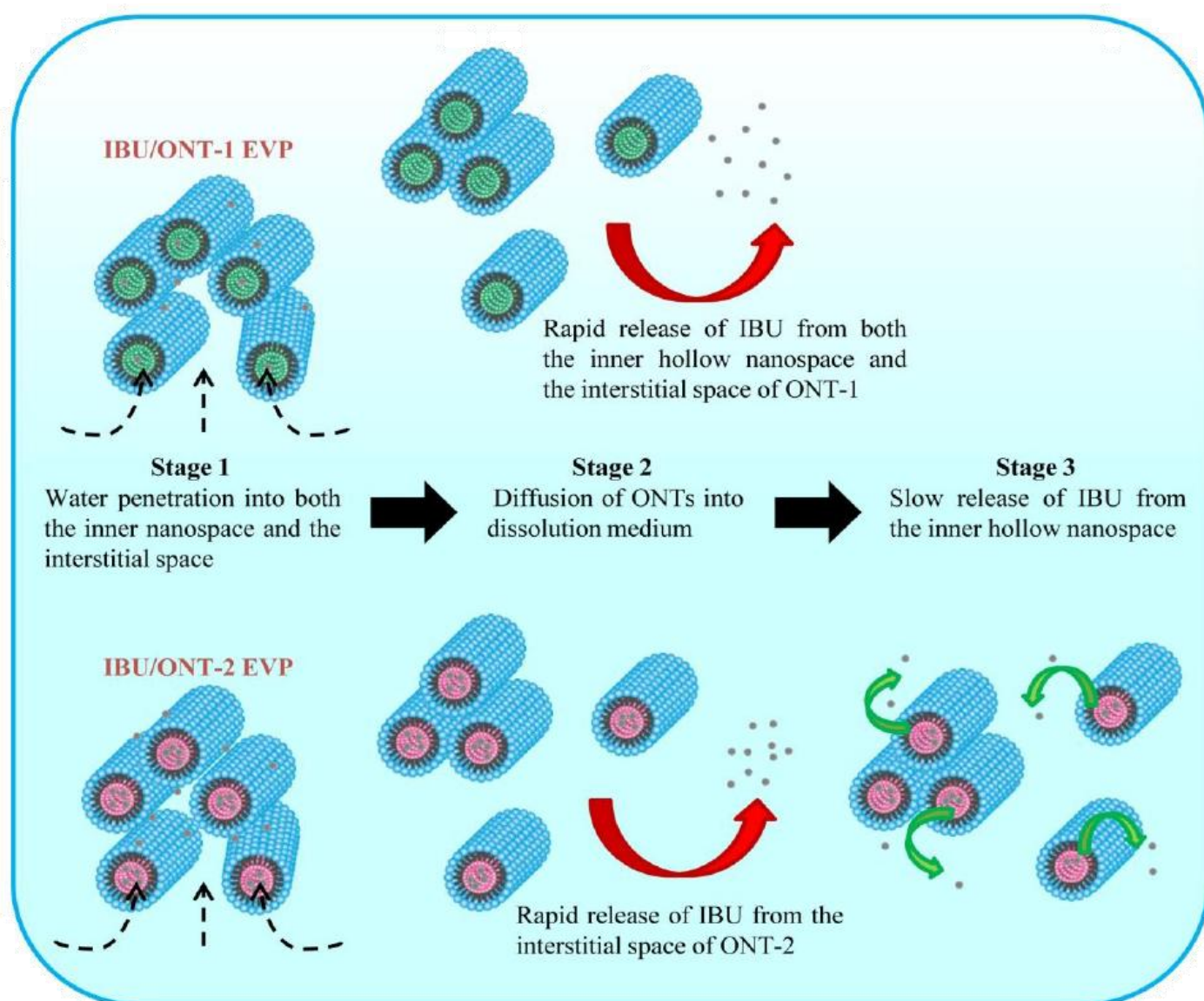


**Figure 3-3.** Schematic illustration of IBU dissolution from IBU/ONT-1 = 1 : 9 EVP (top) and IBU/ONT-2 = 3 : 7 EVP (bottom).

## CONCLUSIONS

The encapsulation of IBU by ONTs was investigated by FE-TEM, PXRD, DSC, and FE-SEM. In addition, multiple solid-state NMR spectroscopies provided insights into the molecular-level interactions between IBU and the ONTs. The molecular states clearly explained the behavior of the IBU encapsulation and dissolution from ONT-1 and ONT-2, which had different functional groups on their surfaces. These findings showed that both ONT-1 and ONT-2 encapsulated IBU not only in their inner hollow nanospace but also on their outer surfaces. The ratio of IBU encapsulation in the inner hollow nanospace versus on the outer surface was 1 : 1 and 2 : 1 for ONT-1 and ONT-2, respectively. IBU encapsulated in the hollow nanospace of both ONTs possessed substantially higher mobility than when attached to the outer surface of the ONTs. The interaction between the carboxyl group of IBU and the glucose hydroxyl group on the outer surface of the ONT was highlighted by 2D HETCOR spectroscopy. The differences in the interaction strengths of IBU/ONT-1 and IBU/ONT-2 affected the amount of IBU encapsulated and the dissolution rate from the different functionalized ONTs. Thus, the encapsulation and dissolution behaviors of guest drugs can be controlled by introducing different functional groups to the surface of host ONTs. This

study clearly illustrates the utility of functionalized ONTs as drug carriers, which can enable controlled encapsulation and dissolution of poorly water-soluble drugs by altering the nature of the host-guest interactions.

## **ACKNOWLEDGEMENTS**

Many people have contributed to development of this research work, which I was very appreciated for their kind cooperation and their advice. First, and foremost, I would like to express my gratitude to my supervisor, Professor Dr. Keiji Yamamoto and Professor Dr. Kunikazu Moribe for their invaluable advice, guidance, encouragement, and understanding throughout my study in Japan.

I wish to express my deep appreciation to Associate Professor Kenjirou Higashi and Assistant Professor Keisuke Ueda for their kindness, advices and encouragement throughout my research.

I would like to express my sincere gratitude to Dr. Junko Kikuchi and Dr. Shigeru Ando of Research Laboratory for Development, Shionogi & Co., Ltd. for solid-state NMR analysis. I would like also thank Dr. Naohiro Kameta, Dr. Wuxiao Ding, Dr. Mitsutoshi Masuda and Dr. Toshimi Shimizu of National Institute of Advanced Industrial Science and Technology (AIST) for supplying of ONTs.

I also wish to thank all members of the Laboratory of Pharmaceutical Technology for their assistance and support all along my study.

This research was partly supported by funding from Grant-in-Aid for Scientific

Research (C) 25460032 and Challenging Exploratory Research 23659017 from the Japan Society for the Promotion of Sciences.

Ultimately, I would like to express my gratitude to my family for their endless love, understanding, encouragement and cheerfulness throughout my study in Japan.

## REFERENCES

1. Shimizu, T.; Masuda, M.; Minamikawa, H., Supramolecular nanotube architectures based on amphiphilic molecules. *Chem. Rev.* **2005**, *105*, 1401–1444.
2. Shimizu, T.; Minamikawa, H.; Kogiso, M.; Aoyagi, M.; Kameta, N.; Ding, W.; Masuda, M., Self-organized nanotube materials and their application in bioengineering. *Polym. J.* **2014**, *46*, 831–858.
3. Kogiso, M.; Aoyagi, M.; Asakawa, M.; Shimizu, T., Highly efficient production of various organic nanotubes with different surfaces and their application to an adsorbent. *Soft Matter* **2010**, *6*, 4528–4535.
4. Song, S.-W.; Hidajat, K.; Kawi, S., Functionalized SBA-15 materials as carriers for controlled drug delivery: influence of surface properties on matrix-drug interactions. *Langmuir* **2005**, *21*, 9568–9575.
5. Qian, K. K.; Zhou, W.; Xu, X.; Udovic, T. J., Characterization of medicinal compounds confined in porous media by neutron vibrational spectroscopy and first-principles calculations: a case study with ibuprofen. *Pharm. Res.* **2012**, *29*, 2432–2444.
6. Yang, P.; Quan, Z.; Lu, L.; Huang, S.; Lin, J., Luminescence functionalization of mesoporous silica with different morphologies and applications as drug delivery

systems. *Biomaterials* **2008**, *29*, 692–702.

7. Vallet-Regí, M.; Balas, F.; Colilla, M.; Manzano, M., Bioceramics and pharmaceuticals: a remarkable synergy. *Solid State Sci.* **2007**, *9*, 768–776.
8. Vallet-Regí, M.; Balas, F.; Arcos, D., Mesoporous materials for drug delivery. *Angew. Chem. Int. Ed.* **2007**, *46*, 7548–7558.
9. Vallet-Regí, M., Ordered mesoporous materials in the context of drug delivery systems and bone tissue engineering. *Chem. Eur. J.* **2006**, *12*, 5934–5943.
10. Kameta, N.; Masuda, M.; Shimizu, T., Soft nanotube hydrogels functioning as artificial chaperones. *ACS Nano* **2012**, *6*, 5249–5258.
11. Kameta, N.; Minamikawa, H.; Masuda, M.; Mizuno, G.; Shimizu, T., Controllable biomolecule release from self-assembled organic nanotubes with asymmetric surfaces: pH and temperature dependence. *Soft Matter* **2008**, *4*, 1681–1687.
12. Kameta, N.; Masuda, M.; Minamikawa, H.; Mishima, Y.; Yamashita, I.; Shimizu, T., Functionalizable organic nanochannels based on lipid nanotubes: encapsulation and nanofluidic behavior of biomacromolecules. *Chem. Mater.* **2007**, *19*, 3553–3560.
13. Wakasugi, A.; Asakawa, M.; Kogiso, M.; Shimizu, T.; Sato, M.; Maitani, Y., Organic nanotubes for drug loading and cellular delivery. *Int. J. Pharm.* **2011**, *413*, 271–278.



14. Ding, W.; Kameta, N.; Minamikawa, H.; Wada, M.; Shimizu, T.; Masuda, M., Hybrid organic nanotubes with dual functionalities localized on cylindrical nanochannels control the release of doxorubicin. *Adv. Healthcare Mater.* **2012**, *1*, 699–706.
15. Chen, H.; Khemtong, C.; Yang, X.; Chang, X.; Gao, J., Nanonization strategies for poorly water-soluble drugs. *Drug Discovery Today* **2011**, *16*, 354–360.
16. Merisko-Liversidge, E.; Liversidge, G. G., Nanosizing for oral and parenteral drug delivery: a perspective on formulating poorly-water soluble compounds using wet media milling technology. *Adv. Drug Delivery Rev.* **2011**, *63*, 427–440.
17. Kameta, N.; Minamikawa, H.; Masuda, M., Supramolecular organic nanotubes: how to utilize the inner nanospace and the outer space. *Soft Matter* **2011**, *7*, 4539–4561.
18. Kameta, N.; Yoshida, K.; Masuda, M.; Shimizu, T., Supramolecular nanotube hydrogels: remarkable resistance effect of confined proteins to denaturants. *Chem. Mater.* **2009**, *21*, 5892–5898.
19. Kameta, N.; Minamikawa, H.; Someya, Y.; Yui, H.; Masuda, M.; Shimizu, T., Confinement effect of organic nanotubes toward green fluorescent protein (gfp) depending on the inner diameter size. *Chem. Eur. J.* **2010**, *16*, 4217–4223.

20. Han, Y.-G.; Aoyagi, M.; Asakawa, M.; Shimizu, T., Facile fabrication and magnetic properties of a one-dimensional magnetite peapod in a lipid nanotube. *ACS Appl. Mater. Interfaces* **2012**, *4*, 2439–2444.
21. Shimizu, T., Self-assembled lipid nanotube hosts: The dimension control for encapsulation of nanometer-scale guest substances. *J. Polym. Sci., Part A: Polym. Chem.* **2006**, *44*, 5137–5152.
22. Higashi, K.; Waraya, H.; Lin, L. K.; Namiki, S.; Ogawa, M.; Limwikrant, W.; Yamamoto, K.; Moribe, K., Application of intermolecular spaces between polyethylene glycol/ $\gamma$ -cyclodextrin-polypseudorotaxanes as a host for various guest drugs. *Cryst. Growth Des.* **2014**, *14*, 2773–2781.
23. Alonso, B.; Marichal, C., Solid-state NMR studies of micelle-templated mesoporous solids. *Chem. Soc. Rev.* **2013**, *42*, 3808–3820.
24. Vogt, F. G.; Roberts-Skilton, K.; Kennedy-Gabb, S. A., A solid-state NMR study of amorphous ezetimibe dispersions in mesoporous silica. *Pharm. Res.* **2013**, *30*, 2315–2331.
25. Ding, W.; Wada, M.; Minamikawa, H.; Kameta, N.; Masuda, M.; Shimizu, T., Cisplatin-encapsulated organic nanotubes by endo-complexation in the hollow cylinder. *Chem. Commun.* **2012**, *48*, 8625–8627.

26. Kameta, N.; Lee, S. J.; Masuda, M.; Shimizu, T., Biologically responsive, sustainable release from metallo-drug coordinated 1D nanostructures. *J. Mater. Chem. B* **2013**, *1*, 276–283.
27. Moribe, K.; Makishima, T.; Higashi, K.; Liu, N.; Limwikrant, W.; Ding, W.; Masuda, M.; Shimizu, T.; Yamamoto, K., Encapsulation of poorly water-soluble drugs into organic nanotubes for improving drug dissolution. *Int. J. Pharm.* **2014**, *469*, 190–196.
28. Tanabe, S.; Higashi, K.; Umino, M.; Limwikrant, W.; Yamamoto, K.; Moribe, K., Yellow coloration phenomena of incorporated indomethacin into folded sheet mesoporous materials. *Int. J. Pharm.* **2012**, *429*, 38–45.
29. Ahmed A.; Barry B.W., Penciclovir solubility in Eudragit films: a comparison of X-ray, thermal, microscopic and release rate techniques. *J. Pharm. Biomed. Anal.* **2004**, *34*, 945–956.
30. Patel, J. R.; Carlton, R. A.; Needham, T. E.; Chichester, C. O.; Vogt, F. G., Preparation, structural analysis, and properties of tenoxicam cocrystals. *Int. J. Pharm.* **2012**, *436*, 685–706.
31. Geppi, M.; Guccione, S.; Mollica, G.; Pignatello, R.; Veracini, C. A., Molecular properties of ibuprofen and its solid dispersions with Eudragit RL100 studied by

- solid-state nuclear magnetic resonance. *Pharm. Res.* **2005**, *22*, 1544–1555.
32. Skorupska, E.; Jeziorna, A.; Paluch, P.; Potrzebowski, M. J., Ibuprofen in Mesopores of Mobil Crystalline Material 41 (MCM-41): A Deeper Understanding. *Mol. Pharmaceutics* **2014**, *11*, 1512–1519.
33. Azaïs, T.; Hartmeyer, G.; Quignard, S.; Laurent, G.; Tourné-Péteilh, C.; Devoisselle, J.-M.; Babonneau, F., Solid-state NMR characterization of drug-model molecules encapsulated in MCM-41 silica. *Pure Appl. Chem.* **2009**, *81*, 1345–1355.
34. Fatnassi, M.; Tourne-Peteilh, C.; Mineva, T.; Devoisselle, J.-M.; Gaveau, P.; Fayon, F.; Alonso, B., Drug nano-domains in spray-dried ibuprofen–silica microspheres. *Phys. Chem. Chem. Phys.* **2012**, *14*, 12285–12294.
35. Azaïs, T.; Tourné-Péteilh, C.; Aussenac, F.; Baccile, N.; Coelho, C.; Devoisselle, J.-M.; Babonneau, F., Solid-state NMR study of ibuprofen confined in MCM-41 material. *Chem. Mater.* **2006**, *18*, 6382–6390.
36. Brás, A. R.; Merino, E. G.; Neves, P. D.; Fonseca, I. M.; Dionísio, M.; Schönhals, A.; Correia, N. T., Amorphous ibuprofen confined in nanostructured silica materials: a dynamical approach. *J. Phys. Chem. C* **2011**, *115*, 4616–4623.
37. Tang, X.-P.; Ng, N. C.; Nguyen, H.; Mogilevsky, G.; Wu, Y., The molecular dynamics and melting transition of the confined ibuprofen in titania nanotube

- studied by NMR. *Chem. Phys. Lett.* **2008**, *452*, 289–295.
38. Izquierdo-Barba, I.; Sousa, E.; Doadrio, J. C.; Doadrio, A. L.; Pariente, J. P.; Martínez, A.; Babonneau, F.; Vallet-Regí, M., Influence of mesoporous structure type on the controlled delivery of drugs: release of ibuprofen from MCM-48, SBA-15 and functionalized SBA-15. *J. Sol-Gel Sci. Technol.* **2009**, *50*, 421–429.
39. Datt, A.; El-Maazawi, I.; Larsen, S. C., Aspirin loading and release from MCM-41 functionalized with aminopropyl groups via co-condensation or postsynthesis modification methods. *J. Phys. Chem. C* **2012**, *116*, 18358–18366.
40. Horcajada, P.; Rámila, A.; Férey, G.; Vallet-Regí, M., Influence of superficial organic modification of MCM-41 matrices on drug delivery rate. *Solid State Sci.* **2006**, *8*, 1243–1249.
41. Babonneau, F.; Yeung, L.; Steunou, N.; Gervais, C.; Ramila, A.; Vallet-Regi, M., Solid state NMR characterisation of encapsulated molecules in mesoporous silica. *J. Sol-Gel Sci. Technol.* **2004**, *31*, 219–223.
42. Sekizaki, H.; Danjo, K.; Eguchi, H.; Yonezawa, Y.; Sunada, H.; Otsuka, A., Solid-State Interaction of Ibuprofen with Polyvinylpyrrolidone. *Chem. Pharm. Bull.* **1995**, *43*, 988–993.
43. Nakazawa, I.; Masuda, M.; Okada, Y.; Hanada, T.; Yase, K.; Asai, M.; Shimizu, T.,

Spontaneous formation of helically twisted fibers from 2-glucosamide bolaamphiphiles: Energy-filtering transmission electron microscopic observation and even-odd effect of connecting bridge. *Langmuir* **1999**, *15*, 4757–4764.

44. Vaisman, L.; Wagner, H. D.; Marom, G., The role of surfactants in dispersion of carbon nanotubes. *Adv. Colloid Interface Sci.* **2006**, *128*, 37–46.
45. Domańska, U.; Pobudkowska, A.; Pelczarska, A.; Gierycz, P., pKa and solubility of drugs in water, ethanol, and 1-octanol. *J. Phys. Chem. B* **2009**, *113*, 8941–8947.

## LIST OF PUBLICATION

This thesis is based on the following publication:

1. Liu, N., Higashi, K., Kikuchi, J., Ando, S., Kameta, N., Ding, W., X., Masuda, M., Shimizu, T., Ueda, K., Yamamoto, K., Moribe, K. Molecular-level understanding of the encapsulation and dissolution of poorly water-soluble ibuprofen by functionalized organic nanotubes using solid-state NMR spectroscopy. *J. Phys. Chem. B.* 2016, 120, 4496-4507.
2. Moribe, K., Makishima, T., Higashi, K., Liu, N., Limwikrant, W., Ding, W., X., Masuda, M., Shimizu, T., Yamamoto, K. Encapsulation of poorly water-soluble drugs into organic nanotubes for improving drug dissolution. *Int. J. Pharm.* 2014, 469, 190-196.

## **THESIS OF COMMITTEE**

This thesis, conducted for the Degree of Doctor of Philosophy (Pharmacy), was examined by the following committee, authorized by the Graduate School of Pharmaceutical Sciences, Chiba University, Japan.

Professor Toshihiko Toida, Ph.D.

(Graduate School of Pharmaceutical Sciences, Chiba University)

Professor Saburo Neya, Ph.D.

(Graduate School of Pharmaceutical Sciences, Chiba University)

Professor Hidetaka Akita, Ph.D.

(Graduate School of Pharmaceutical Sciences, Chiba University)

Professor Ashfaq Mahmood, Ph.D.

(Graduate School of Pharmaceutical Sciences, Chiba University)